

1 **Assessment of the impact of spatial heterogeneity on**
2 **microwave satellite soil moisture periodic error**

3 **Fangni Lei^{a,b}, Wade T. Crow^a, Huanfeng Shen^b, Chun-Hsu Su^c, Thomas R. H. Holmes^d,**
4 **Robert M. Parinussa^e, Guojie Wang^f**

5
6 ^a*USDA ARS Hydrology and Remote Sensing Laboratory, Beltsville, MD 20705, USA*

7 ^b*School of Resource and Environmental Sciences, Wuhan University, Wuhan, Hubei 430072, China*

8 ^c*Department of Infrastructure Engineering, University of Melbourne, Parkville, Victoria 3010, Australia*

9 ^d*NASA GSFC Hydrological Sciences Laboratory, Greenbelt, MD 20771, USA*

10 ^e*Transmissivity B.V./VanderSat B.V., Space Technology Business Park, Huygenstraat 34, Noordwijk 2201*
11 *DK, The Netherlands*

12 ^f*School of Geography and Remote Sensing, Nanjing University of Information Science and Technology,*
13 *Nanjing, Jiangsu 210044, China*

14

15

16 **Abstract:**

17 An accurate temporal and spatial characterization of errors is required for the efficient processing,
18 evaluation, and assimilation of remotely-sensed surface soil moisture retrievals. However,
19 empirical evidence exists that passive microwave soil moisture retrievals are prone to periodic
20 artifacts which may complicate their application in data assimilation systems (which commonly
21 treat observational errors as being temporally white). In this paper, the link between such
22 temporally-periodic errors and spatial land surface heterogeneity is examined. Both the synthetic
23 experiment and site-specified cases reveal that, when combined with strong spatial heterogeneity,
24 temporal periodicity in satellite sampling patterns (associated with exact repeat intervals of the
25 polar-orbiting satellites) can lead to spurious high frequency spectral peaks in soil moisture
26 retrievals. In addition, the global distribution of the most prominent and consistent 8-day spectral
27 peak in the Advanced Microwave Scanning Radiometer – Earth Observing System soil moisture
28 retrievals is revealed via a peak detection method. Three spatial heterogeneity indicators – based
29 on microwave brightness temperature, land cover types, and long-term averaged vegetation index
30 – are proposed to characterize the degree to which the variability of land surface is capable of
31 inducing periodic error into satellite-based soil moisture retrievals. Regions demonstrating 8-day
32 periodic errors are generally consistent with those exhibiting relatively higher heterogeneity
33 indicators. This implies a causal relationship between spatial land surface heterogeneity and
34 temporal periodic error in remotely-sensed surface soil moisture retrievals.

35

36 **Keywords:**

37 Microwave remote sensing; Satellite-derived soil moisture; Spectral analysis; Periodicity; Spatial
38 heterogeneity

39 **I. Introduction**

40 Within the past two decades, extensive efforts have been aimed at enhancing remote
41 estimation of surface soil moisture. Currently, several global space-borne soil moisture products
42 are available from a series of satellite-based passive and/or active microwave sensors. The accurate
43 characterization of global satellite-derived soil moisture products is crucial for multiple
44 hydrological (Srivastava et al., 2013; Wagner et al., 2007a), meteorological (Koster et al., 2004;
45 Seneviratne et al., 2010), agricultural (Bolten et al., 2010; Engman et al., 1991; Lakhankar et al.,
46 2009a), and natural hazardous (Lacava et al., 2005) applications. Especially in hydrological data
47 assimilation community, the inclusion of satellite-based soil moisture observations has drawn great
48 attention for the purposes of catchment rainfall-runoff (Alvarez-Garreton et al., 2014; Crow et al.,
49 2009; Komma et al., 2008) and both continental (Crow and Zhan, 2007; Walker and Houser, 2004)
50 and global-scale (Reichle and Koster, 2005; Reichle et al., 2004; 2007) land surface modeling.

51 Recently, Su et al. (2013a; 2015) presented a spectrally-based approach for evaluating
52 satellite-derived soil moisture retrievals, which builds upon a semi-empirical water balance model
53 and operates in the frequency domain. Based on this approach, they identified periodic error
54 components in passive microwave retrieved soil moisture Level 3 (gridded) retrieval products
55 acquired from both the Advanced Microwave Scanning Radiometer – Earth Observing System
56 (AMSR-E) and the Soil Moisture and Ocean Salinity (SMOS) missions, suggesting the need to
57 consider the presence of temporally-periodic errors when using and/or evaluating such products.
58 Most land data assimilation approaches are based on an assumption of temporally-white and
59 Gaussian-distributed errors forms (Burgers et al., 1998). Therefore, a thorough examination of soil
60 moisture retrieval error structure is crucial for not only properly describing their error

61 characteristics but also their potential implementation within a land data assimilation system
62 (Crow and Van den Berg, 2010).

63 Gridded satellite-based soil moisture retrievals are based on the sampling of adjacent
64 footprints within the same orbital overpass. Three commonly used interpolation algorithms are:
65 drop-in-bucket, nearest neighbor, and inverse-distance-squared methods (Chan et al., 2012). The
66 choice of interpolation algorithm affects the effective antenna pattern of the spatial support
67 associated with a particular grid box. For the Soil Moisture Active Passive (SMAP) mission, the
68 averaged half-power beam-width field-of-view (FOV) size of the inverse-distance-squared
69 approach is about 40 km. In addition, radiation outside the half-power beam-width can contribute
70 to the signal – suggesting that the gridded signal may include significant radiance contributions
71 from emitters outside the grid (Jackson et al., 2010). For polar-orbiting satellites with an exact
72 repeat cycle there are periodic variations in the spatial support of individual grids (due to day-to-
73 day variations in the exact footprint-averages underlying each grid cell). Over highly
74 heterogeneous regions, the impact of this periodic sampling may become more pronounced and
75 periodic errors may arise which are related to the periodicity of the sampling pattern.

76 Additionally, passive microwave observations are potentially contaminated by man-made
77 radio frequency interference (RFI). RFI can obscure (relatively weaker) geophysical emission
78 associated with land source variables like soil moisture (Daganzo-Eusebio et al., 2013; Njoku et
79 al., 2005). In addition to the spatial heterogeneity in natural land surface signals, RFI sources
80 observed over land areas are typically fixed in space (Njoku et al., 2005) which may lead to
81 periodic errors in satellite-based retrievals as these sources are re-sampled periodically. From this
82 point of view, a satellite-derived soil moisture product with consideration of the contributing factor
83 of RFI should be analyzed to expose the origins of periodic errors.

84 In practice, a simple *ad hoc* low pass filter (i.e., a 5-day moving average) adopted by
85 Wagner et al. (2007b) and Draper et al. (2009) has been shown to slightly improve the quality of
86 satellite-based soil moisture retrievals. Nonetheless, this empirical method is arbitrary and only
87 effective for dampening very short-term fluctuations (i.e., 2-day periodic errors). Recent
88 experimental studies have shown that analyzing the soil moisture time series in the frequency
89 domain can provide supplementary insights with regard to its conjugate time domain (Katul et al.,
90 2007). For example, Du (2012) used the high-pass Fourier filter to keep small temporal scale soil
91 moisture signals in the directly observed emissivity time series, while filtering out the mixture
92 signals of vegetation phenology in the low frequency component (Moody and Johnson, 2001;
93 Scharlemann et al., 2008) and long-term soil moisture trends. However, such a method requires
94 not only the accurate extraction of high-frequency soil moisture signals from sensor direct
95 observations, but also the availability of an accurate long-term climatology from land surface
96 models or existing satellite-based soil moisture product. On the other hand, Su et al. (2013a)
97 applied a band-stop filter to remove the identifiable stochastic and systematic errors in high-
98 frequency regime and then a low-pass Wiener filter for preserving the long-term temporal mean
99 and variance. This approach is more physically realistic and based on the rationale that small time
100 scale soil moisture dynamics can be simplified into incoming precipitation and water loss process
101 with brown-like spectrum (Katul et al., 2007; Su et al., 2013a).

102 However, the application of any filter comes at the risk of information loss. For example,
103 when blindly applying the band-stop filter, high-frequency signal components related to rapid soil
104 moisture changes following intense rainfall events can also be attenuated. Therefore, the accurate
105 *a priori* identification of land surface conditions associated with spurious high frequency
106 resonances is beneficial for efficient and flexible application of the band-stop filter.

107 To examine the plausible reasons behind the existence of high-frequency peaks and
108 improve our understanding of errors in the satellite-derived soil moisture time series, this study
109 will focus primarily on the most prominent and consistent periodicity (8-day) existing in an
110 AMSR-E soil moisture retrieval product. The spatial distribution of such a periodic error will be
111 inter-compared to measures of land surface spatial heterogeneity. Section 2 presents the satellite-
112 derived soil moisture product from the passive microwave AMSR-E sensor via the Land Parameter
113 Retrieval Model (LPRM) retrieval algorithm, the spectral analysis of soil moisture, and our peak
114 detection method. Three straightforward heterogeneity indicators, based on: microwave brightness
115 temperature, land cover types, and long-term averaged Normalized Difference Vegetation Index
116 (NDVI), are then proposed for characterizing spatial variability along the land surface. Section 3
117 evaluates the spectral characteristics of soil moisture retrievals and explains their relationship with
118 these heterogeneity indicators. Further discussion of concerns and potential implications is
119 provided in section 4, and final conclusions are presented in section 5.

120

121 **II. Materials and methods**

122 A long-term soil moisture product is necessary in order to robustly investigate periodic
123 errors in satellite-derived soil moisture time series. Among various microwave sensors and
124 missions, the AMSR-E sensor onboard the National Aeronautics and Space Administration
125 (NASA) Aqua provides the longest currently-available source of soil moisture data (i.e., from June
126 2002 to October 2011) from a single sensor and is therefore the primary focus of this study.

127

128 *2.1. AMSR-E soil moisture product and LPRM retrieval model*

129 *2.1.1 AMSR-E basic information*

130 The AMSR-E sensor was a six-frequency dual-polarized passive microwave radiometer,
131 onboard the NASA Aqua satellite with a 16-day exact repeat cycle. With a sun-synchronous orbit
132 at an altitude of 705 km, AMSR-E scans the Earth's surface at 1:30 a.m. (descending)/1:30 p.m.
133 (ascending) local equator overpass time and an incidence angle of 55°. AMSR-E provided a nearly
134 nine-and-a-half-years long-term measurement time series from June 2002 to October 2011.
135 Among its six microwave frequency bands, the spatial resolutions of footprint measurements at
136 6.9 GHz (C-band), 10.7 GHz (X-band), and 36.5 GHz (Ka-band) were 74 ×43 km, 51×30 km,
137 and 14×8 km, respectively (Njoku et al., 2003).

138 Several soil moisture retrieval algorithms have been developed for AMSR-E brightness
139 temperature (T_B) data. Here, surface soil moisture (~2 cm) and vegetation optical depth are
140 retrieved simultaneously from C-band T_B via the LPRM (see below for further details). In areas
141 with significant RFI such as the contiguous United States (CONUS), Japan, and India, LPRM
142 switches to X-band. [Figure 1.a and 1.b show the distribution maps of bands that have been utilized](#)
143 [for soil moisture retrieval](#). Regardless of the band used, AMSR-E ascending and descending half-
144 orbits are separately re-sampled from their original footprint resolution to a regular quarter degree
145 grid and then processed through LPRM to retrieve soil moisture (see below).

146 *2.1.2 Land Parameter Retrieval Model*

147 LPRM uses a forward modeling optimization procedure to solve a radiative transfer
148 equation without the need for parameter calibration and other biophysical measurements. The
149 physically-based LPRM (De Jeu and Owe, 2003; Meesters et al., 2005; Owe et al., 2001) has been
150 successfully applied to retrieve surface soil moisture from space-borne passive microwave
151 observations including AMSR-E (Owe et al., 2008) and SMOS (De Jeu et al., 2009; Van der
152 Schalie et al., 2015; Van der Schalie et al., 2016). Moreover, the AMSR-E LPRM product has

153 been well-validated with *in situ* campaigns (Brocca et al., 2011; De Jeu et al., 2008; Draper et al.,
 154 2009; Su et al., 2013b) and thoroughly assessed in previous studies (Al-Yaari et al., 2014; Dorigo
 155 et al., 2010; Draper et al., 2012; Rebel et al., 2012). Here, version 5 of the AMSR-E LPRM soil
 156 moisture product is collected from January 2003 to October 2011.

157 The LPRM algorithm can simultaneously retrieve surface soil moisture and vegetation
 158 optical depth (VOD) from passive microwave observations using both horizontally- and vertically-
 159 polarized T_B data. The retrieval scheme is based on solving a radiative transfer model (Mo et al.,
 160 1982) via a nonlinear iterative optimization procedure. The radiation emission T_b measured over
 161 a land surface with vegetation canopy can be described as

$$162 \quad T_{b(P)} = T_S e_{r(P)} \Gamma_V + (1 - \omega) T_C (1 - \Gamma_V) + (1 - e_{r(P)}) (1 - \omega) T_C (1 - \Gamma_V) \Gamma_V \quad (1)$$

163 where the subscript P is H for horizontal or V for vertical polarization, T_S the thermodynamic soil
 164 temperature, $e_{r(P)}$ the rough surface emissivity, Γ_V the vegetation transmissivity, ω the single
 165 scattering albedo, and T_C the canopy temperature. The above equation represents three terms: the
 166 radiation emanated from the underlying soil as attenuated by the canopy, the upward radiation
 167 directly from the overlying vegetation, and the downward radiation from the vegetation (reflected
 168 by the soil and further attenuated by the vegetation).

169 The rough surface emissivity is calculated for both polarizations using the emissivity model
 170 developed by Wang and Choudhury (1981)

$$171 \quad e_{r(H)} = 1 - ((1 - Q)R_{s(H)} + QR_{s(V)})e^{-h\cos(u)} \quad (2)$$

172 where Q and h are the polarization mixing factor and empirical roughness, respectively, and both
 173 are dimensionless parameters. The smooth surface reflectivity R_s is a function of dielectric
 174 constant k and satellite observational incidence angle u and is calculated using the Fresnel
 175 equations. Furthermore, the dielectric constant k is estimated via the Wang-Schmugge dielectric

176 mixing model (Wang and Schmugge, 1980). Equation 2 is written for H polarization emissivity.
177 For V polarization results, the polarization signs should be switched.

178 The vegetation transmissivity Γ_V is defined in terms of the VOD τ_V and incidence angle u
179 as

$$180 \quad \Gamma_V = \exp\left(\frac{-\tau_V}{\cos(u)}\right) \quad (3)$$

181 The VOD τ_V is directly related to the canopy density, or more specifically, the vegetation water
182 content. Derived by Meesters et al. (2005), the VOD is a function of k and the Microwave
183 Polarization Difference Index (*MPDI*)

$$184 \quad MPDI = \frac{T_{b(V)} - T_{b(H)}}{T_{b(V)} + T_{b(H)}} \quad (4)$$

185 where *MPDI* is calculated directly from observed brightness temperatures. By normalizing for
186 temperature dependence, the *MPDI* becomes more highly-related to the dielectric properties of the
187 radiating body including both the canopy and soil emissions (Owe et al., 2008).

188 Regarding the thermodynamic conditions of vegetation and soil, a further assumption in
189 the LPRM algorithm is that the soil temperature and canopy temperature are in isothermal
190 equilibrium

$$191 \quad T_S = T_c = T \cong aT_{b(V)}^{Ka} + b. \quad (5)$$

192 For AMSR-E, T is derived from the accompanying Ka-band T_b at V polarization (Holmes et al.,
193 2009). Atmospheric contributions to satellite observed T_B are also taken into account following
194 Owe et al. (2008).

195

196 **2.2. Ancillary dataset**

197 **2.2.1 International Soil Moisture Network**

198 The International Soil Moisture network (ISMN) has assembled over 50 operational and
199 experimental soil moisture networks worldwide, providing a global *in situ* soil moisture database
200 with uniform data format and pre-processing quality flags (Dorigo et al., 2013). While most of the
201 networks are located in northern America and Europe, some regions in Asia and Australia are also
202 covered. Detailed information about the ISMN is reported in Dorigo et al. (2011) and Gruber et al.
203 (2013). The ISMN dataset was downloaded from <http://ismn.geo.tuwien.ac.at> in February 2017.

204 For direct comparison with AMSR-E LPRM soil moisture product, these sparsely
205 distributed *in situ* soil moisture records are analyzed in the frequency domain as well. The ISMN
206 soil moisture is originally recorded along with Coordinated Universal Time (UTC) time and has
207 been converted to local solar time before next processing. To be consistent with the overpass time
208 of AMSR-E, records are extracted at 02:00 p.m. and 01:00 a.m. for ascending and descending half-
209 orbits, respectively. Observations are masked using the quality flag (identified as ‘good’ with ‘G’)
210 and stations located within the same quarter degree box are averaged for simplicity. For example,
211 there are three networks of which 55 stations are collocated within a quarter degree grid (latitude:
212 38.375° N, longitude: 120.875° W), namely COSMOS, FLUXNET-AMERIFLUX, and
213 SOILSCAPE. However, only three stations provided measurements during our study period and
214 are averaged accordingly. Note that the point-scale soil moisture observation cannot fully represent
215 the footprint satellite retrieval and the sampling depth may also introduce differences. Strategies
216 have been proposed for minimizing the systematic differences between ground-based
217 measurement and satellite-based retrievals, such as computing anomalies through subtracting a
218 moving window averaging-based climatology (Dorigo et al., 2015; Gruber et al., 2013). However,
219 since the *in situ* soil moisture is used only to help identifying spectral peaks in AMSR-E
220 LPRM soil moisture retrievals, these strategies have not been applied here.

221 *2.2.2 Land cover—GlobeLand30*

222 Several global land cover maps derived from multiple satellite sensors are currently
223 available. The sensitivity of microwave emissivity to soil moisture varies with different land cover
224 variables – in particular, vegetation optical depth. High spatial resolution surface land cover maps
225 can thus provide sub-pixel heterogeneity information for coarse resolution soil moisture products.
226 However, the isolation of highly mixed land cover types is cumbersome and beyond the scope of
227 this study. Therefore, the 30-meters high resolution GlobeLand30 dataset, based on Landsat data
228 (Chen et al., 2015), is merely included for visual interpretation of the spatial heterogeneity within
229 the quarter degree grid of AMSR-E LPRM soil moisture retrievals. According to previous
230 independent accuracy assessments, the GlobeLand30 has demonstrated an overall accuracy of over
231 80% (Brovelli et al., 2015). It was downloaded from <http://globallandcover.com> in January 2017.

232 *2.2.3 Normalized Difference Vegetation Index (NDVI)—MODIS*

233 The Moderate Resolution Imaging Spectroradiometer (MODIS) monthly NDVI
234 (MOD13C2) product is obtained from January 2003 to December 2011. To be consistent with
235 AMSR-E LPRM soil moisture retrievals, it has been spatially-aggregated from its original 0.05°
236 grid to a regular 0.25° resolution. A long-term averaged global NDVI distribution map is then
237 generated by averaging all quarter-degree monthly data. The MOD13C2 dataset was downloaded
238 from https://lpdaac.usgs.gov/dataset_discovery/modis/modis_products_table/mod13c2_v006
239 during May 2017.

240 *2.2.4 Land cover type—MODIS*

241 In addition to the high resolution land cover from the GlobeLand30 product, a dominant
242 land cover type map at lower spatial resolution (0.05°) is acquired from the MODIS yearly Land
243 Cover Type Climate Modeling Grid (MCD12C1) product in 2011. This product also provides the

244 sub-grid frequency distribution of land cover types. Three classification schemes are included and
245 the primary International Geosphere Biosphere Programme (IGBP) land cover scheme is selected
246 for further analysis. IGBP contains 17 land cover classes and has been re-classified into 9 classes
247 before spatially-aggregated to regular quarter degree (0.25°). They are: Water, Forest, Shrublands,
248 Grasslands, Cultivated Land, Wetlands, Artificial Surfaces, Permanent Snow and Ice, and
249 Bareland. Percentages of difference land cover types are summed for each quarter-degree box and
250 normalized to [0,100]. The MCD12C1 dataset was downloaded from [https://lpdaac.](https://lpdaac.usgs.gov/dataset_discovery/modis/modis_products_table/mcd12c1)
251 [usgs.gov/dataset_discovery/modis/modis_products_table/mcd12c1](https://lpdaac.usgs.gov/dataset_discovery/modis/modis_products_table/mcd12c1) during May 2017.

252

253 ***2.3. Spectral frequency analysis and peak detection method***

254 *2.3.1 Power spectral density estimation*

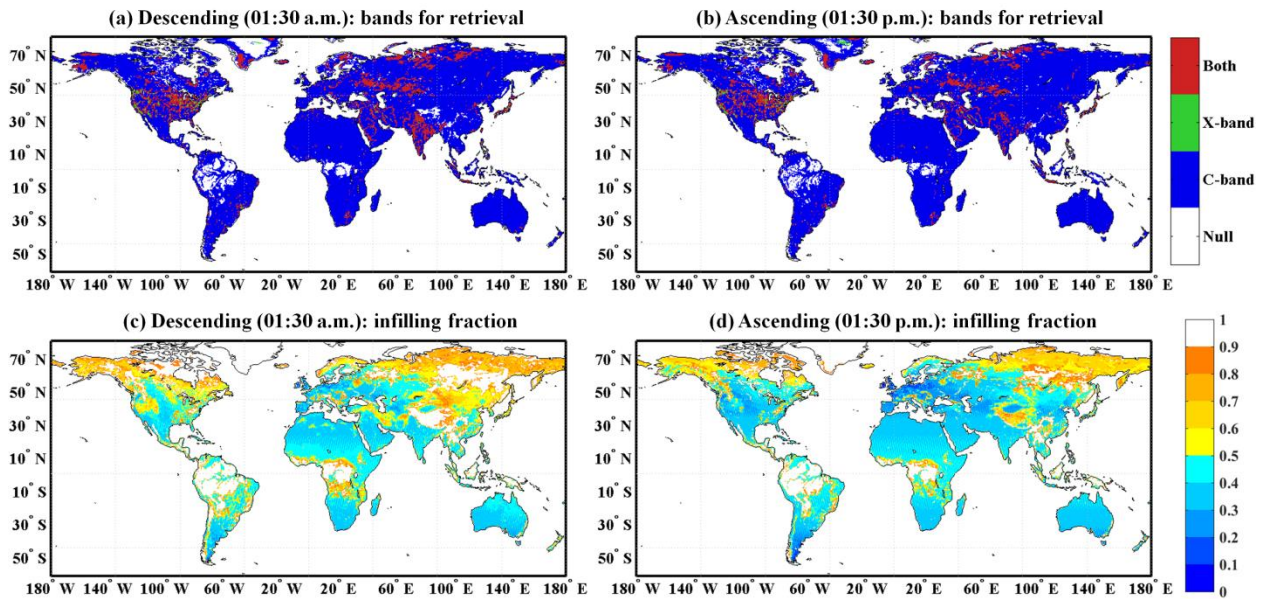
255 The dynamics of soil moisture is an outcome of interactions between incoming
256 precipitation, canopy interception, evapotranspiration, surface runoff, lateral flow and
257 groundwater. The near-surface soil moisture time series consists of both a long-term climatology
258 (low frequency) and short-term anomaly (high frequency) components (Entin et al., 2000). The
259 long-term climatology originates from seasonally varying precipitation and solar radiation and can
260 be affected by the vegetation phenology, climate change, and instrument drift for satellite
261 observations. In contrast, the short-term anomalies represent the process of rainfall instances and
262 dry-down events and are valuable for analyzing short-term weather extremes (Katul et al., 2007;
263 Wu and Dickinson, 2004). However, this short-term information is usually contaminated by
264 observational noises and systematic errors. Here, we focus on the periodic error in the high-
265 frequency regime which may be introduced by the satellite orbiting pattern and/or gridding
266 approach.

267 Following the approach of Su et al. (2013a; 2015), the power spectral density (PSD, in unit
268 of $\text{m}^6/\text{m}^6 \text{ 24hr/rad}$) of AMSR-E LPRM soil moisture retrievals at a given grid is estimated using
269 the Welch's averaged modified periodogram method. This method computes a modified
270 periodogram for each temporal segment separated by a moving Hamming window and averages
271 over all estimates to produce a single PSD. Note that the size of Hamming window can play a role
272 in determining the PSD estimation. Wider Hamming windows tend to produce higher spectral
273 resolution in the estimated PSD but greater uncertainty in the amplitude estimation, while shorter
274 windows provide coarser spectral resolution but with lower uncertainty in amplitude. The impact
275 of Hamming window size on key results will be clarified when describing the peak detection
276 method in section 2.3.4.

277 Another issue with PSD estimation is satellite overpass time. AMSR-E has a ascending
278 half-orbit at 1:30 p.m. and descending half-orbit at 1:30 a.m. Considering that the FOV and near-
279 surface thermal conditions (more specifically, the temperature contrast across the soil-vegetation-
280 air interface) are quite different for these two half-orbits, soil moisture retrievals from ascending
281 and descending overpasses have been separately analyzed with periodic temporal sampling along
282 a 24 h interval.

283 In applying the Fourier transform to stationary time series, most standard PSD estimation
284 algorithms – including Welch's method – require an evenly sampled dataset in time. However,
285 temporal data gaps in passive microwave satellite-derived soil moisture product are inevitable –
286 primarily due to the satellite orbits, dense vegetation, RFI contamination, and masking for frozen
287 soil conditions. In this particular case, AMSR-E LPRM soil moisture retrievals are masked if the
288 complementary VOD levels exceeded 0.8—a level at which the soil radiation is substantially
289 masked out by the canopy (Owe et al., 2008; De Jeu et al., 2008; Parinussa et al., 2011). Further

290 masking has been conducted for grids with significant RFI contamination (Li et al., 2004) and for
 291 frozen soil conditions. In order to produce evenly-spaced data after the application of this masking,
 292 the 1-D Discrete Cosine Transform (DCT) method (Garcia, 2010) is applied for infilling missing
 293 values in the AMSR-E LPRM soil moisture time series. In this study, only grids with less than 365
 294 observations during the 9-years experiment period (11%) are omitted to preserve sufficient spatial
 295 coverage for global analysis with indication of highly in-filled regions. Figure 1.c and Figure 1.d
 296 show the fraction of in-filled data in the AMSR-E LPRM soil moisture product for both descending
 297 and ascending retrievals. Due to the generally warmer surface conditions during the ascending
 298 (01:30 p.m.) half-orbit (Holmes et al., 2015), the fraction of data gaps in descending overpasses is
 299 slightly higher than its ascending counterpart. Additional discussion and an assessment of the
 300 infilling method can be found in section 4.2 and section A of the supporting materials.



301
 302 **Figure 1.** Spatial distribution maps of applied bands for AMSR-E LPRM soil moisture retrieval (upper row) and
 303 fraction of in-filled data for the period 2003 – 2011 (bottom row): (a) and (c) for descending; (b) and (d) for ascending
 304 overpasses, respectively.

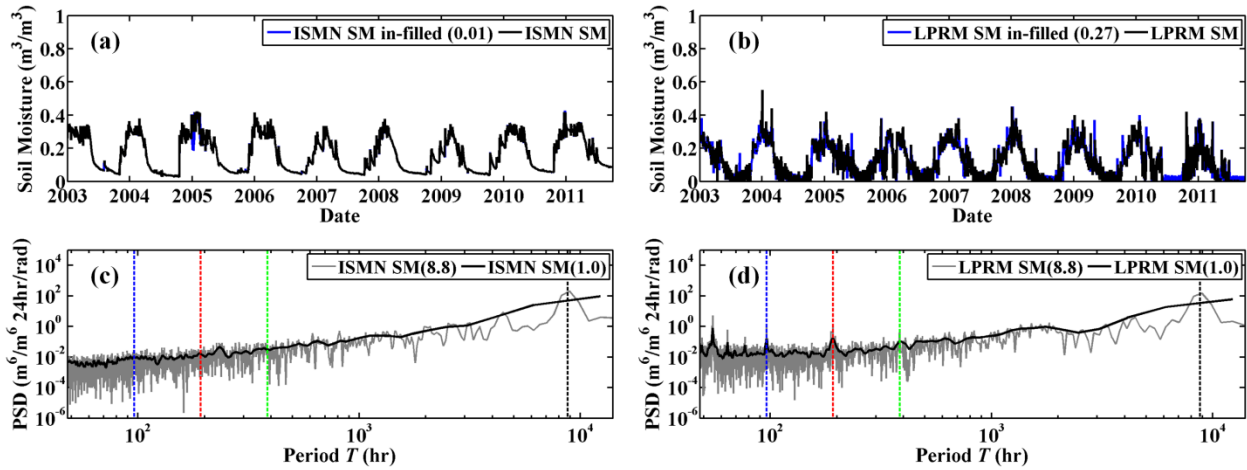
305 *2.3.2 Spectrum characteristics of soil moisture time series*

306 Figure 2 shows the AMSR-E LPRM and ISMN *in situ* soil moisture time series from
307 January 2003 to October 2011 for a single 0.25° grid (latitude: 38.375° N, longitude: 120.875° W).
308 Corresponding PSDs are estimated with two Hamming window sizes (i.e., 1.0 and 8.8 in units of
309 year).

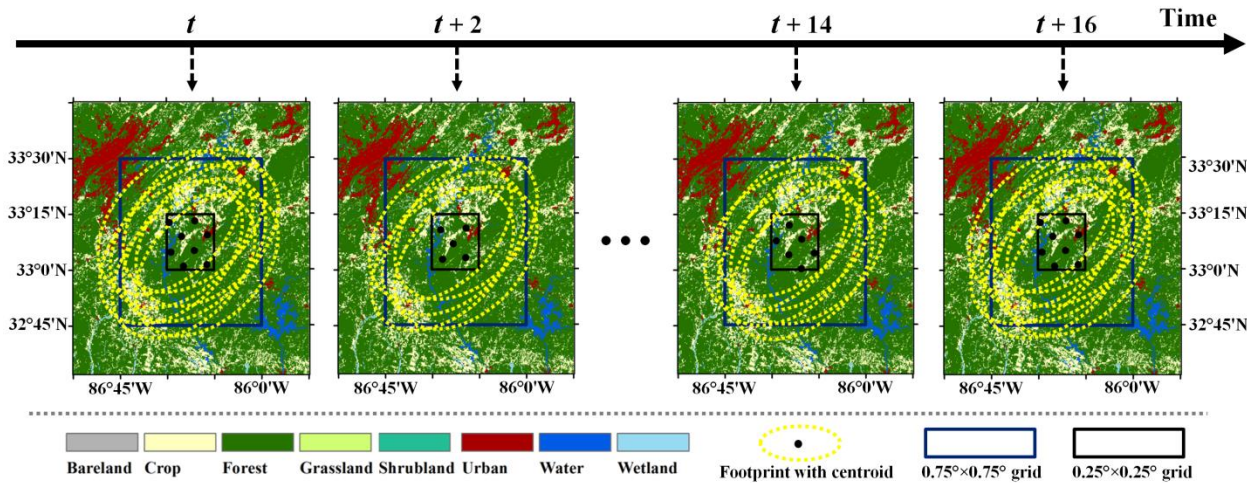
310 According to Katul et al. (2007), the soil water balance model dictates that the soil moisture
311 time series exhibits a Brownian spectrum with more energy at lower frequency and a decrease in
312 power with increasing frequency (Figure 2.c). Comparing the PSDs of footprint AMSR-E LPRM
313 soil moisture retrievals and point-scale *in situ* observations, significant discrepancies exist at high
314 frequencies. In particular, the relatively flat power distributions of AMSR-E LPRM soil moisture
315 for $T < 10^3$ h reflect high-frequency noise, which can be introduced by various short-term stochastic
316 processes contributing to retrieval errors (Su et al., 2013a). Note that – based on a thorough
317 exploration over various grids with *in situ* soil moisture observations – the grid demonstrated here
318 is representative for a spectral comparison between ground-based measurements and satellite-
319 derived soil moisture retrievals.

320 Importantly, several distinct resonant peaks with periods ranging between 2 to 16 days are
321 sitting on the AMSR-E flat noise floor (Figure 2.d). Given the lack of known physical processes
322 capable of producing such harmonics, these peaks are likely spurious signals characterized by
323 periodic increases in power with these time intervals. Without consideration of the long-term
324 satellite orbit drift, the repeat cycle of AMSR-E is 16 days which means that the sensor observes
325 exactly the same region every 16 days. Within this 16-day period, there are periodic variations in
326 the locations of antenna footprints sampled to capture a grid-cell mean (as shown in Figure 3). Our
327 hypothesis is that this kind of periodic sampling pattern can generate spectral peaks within highly

328 heterogeneous regions. If true, it implies that spectral peaks can be connected to strong – and
 329 temporally stable – patterns of land surface heterogeneity.



330
 331 **Figure 2.** The soil moisture time series (a and b) and corresponding power spectral density (PSD, c and d) of both
 332 ISMN *in situ* and AMSR-E LPRM soil moisture data at the ascending overpass time (01:30 p.m.). The infilling
 333 fractions of soil moisture data are shown in the brackets and the Hamming window sizes for PSD estimation inside
 334 the brackets are in units of year. From left to right, the dotted vertical lines represent periods at 4-day (blue), 8-day
 335 (red), 16-day (green), and 365-day (black).



336
 337 **Figure 3.** An illustration of the time-varying effective spatial support for a single quarter degree grid (centered at
 338 33.125° N, 86.375° W and outlined with a black square) where multiple adjacent footprints (yellow dotted ellipses)
 339 within the same orbital overpass are averaged. The background land cover maps are projected in World Geodetic

340 System (WGS) 1984 Universal Transverse Mercator (UTM) zone 16 North system. Comparing time t and $t + 16$, the
341 satellite observes exactly the same region.

342 2.3.3 Examining the occurrence of periodic errors

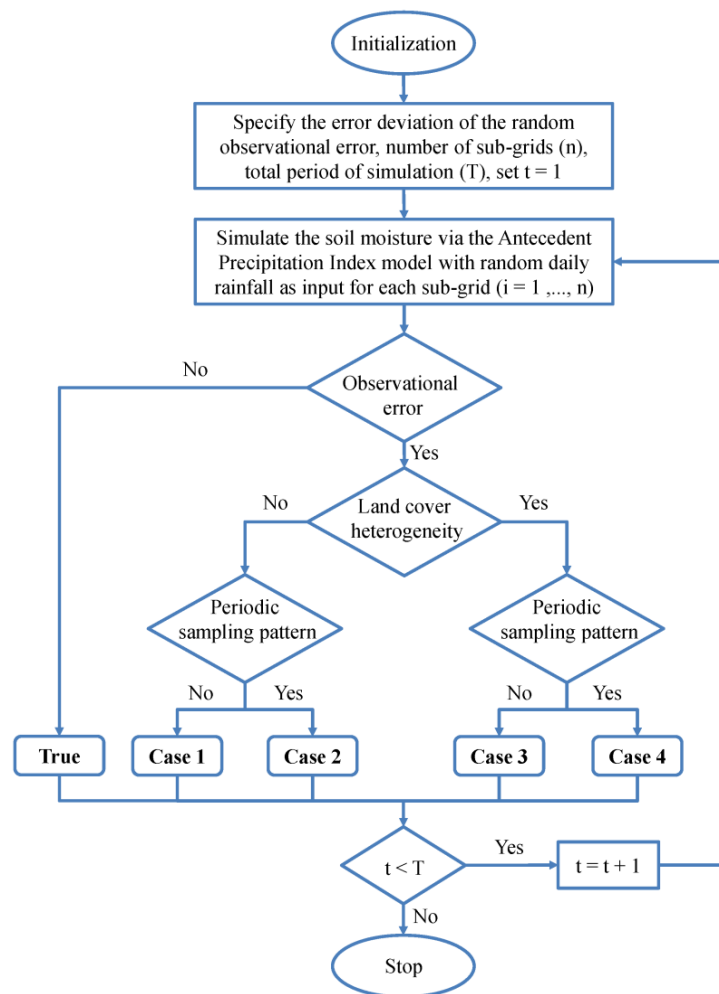
343 To further facilitate the physical interpretation of the occurrence of high-frequency peaks,
344 a simplistic synthetic experiment monitoring the periodic sampling pattern of satellite swaths over
345 different land cover characteristics has been conducted following the approach illustrated in Figure
346 4. In particular, an Antecedent Precipitation Index (API) model is applied to generate synthetic
347 soil moisture $SM_{t,i}$ (mm, in a dimension of water depth) for each sub-grid i at time t

$$348 \quad SM_{t,i} = \gamma SM_{t-1,i} + P_t \quad i = 1, \dots, n \quad (6)$$

349 where γ is a dimensionless API loss coefficient and assumed to be a constant value as 0.95; n is
350 the total number of sub-grids which is set to 9 (3-by-3), and P_t (mm) represents the daily
351 accumulation depth of random rainfall expressed in dimensions of water depth and generated from
352 the exponential distribution with mean of 25 mm.

353 In total, there are five synthetic scenarios (see Figure 4). The synthetic “True” soil moisture
354 is generated directly through the API model without any assumed observational error, while mean-
355 zero Gaussian distributed random observational error with a standard deviation of 10 mm is added
356 to the other four cases. With the consideration of spatial heterogeneity, a long-term bias in soil
357 moisture within the 3-by-3 grid box is set up as a random pattern from a mean-zero normal
358 distribution with a standard deviation of 20 mm. This long-term bias is meant to represent the
359 systematic land cover and/or soil physical property variations. Furthermore, the periodic sampling
360 pattern of satellite footprints is constructed by repeating equally-weighted averaging with different
361 combinations of sub-grids (to account for the drop-in-bucket method use in the AMSR-E LPRM
362 product). In accordance with AMSR-E, the repeat cycle is set to 16-days. Through the combination
363 of these two conditions, four experiments are generated (see Figure 4). Here, the differences in

364 mean and standard deviation settings among precipitation, soil moisture observational error and
 365 long-term bias only represent their scaling differences and proportionally rescaling these statistical
 366 moments does not affect presented results. Before the spectral frequency analysis, five synthetic
 367 soil moisture time series (four Cases and “True”) are normalized respectively from their original
 368 climatology to be mean-zero with a standard deviation of one. These synthetically-generated
 369 results will be used to enhance our understanding of peak-generating processes within our real-
 370 data analysis. Results from these synthetic experiments will be presented in section 3.1.



371
 372 **Figure 4.** Flowchart of synthetic experiments which examine the combined impact of land surface heterogeneity and
 373 periodic orbital sampling pattern on producing spectral harmonics.

374 2.3.4 Detection of 8-day periodic error

375 With a Brownian spectrum of soil moisture, the increase in power with decreasing
376 frequency may hinder detection of 16-day peaks in cases where the true soil moisture signal is
377 stronger than the 16-day resonance. In addition, spectral peak features in higher frequencies can
378 be difficult to be distinguished from the high-frequency noise. Therefore, despite the fact that
379 AMSR-E LPRM soil moisture retrievals demonstrate several spectral resonances, we will focus
380 on 8-day peaks as they represent the most prominent and consistent periodic signal. Detailed peak
381 detection procedures are described below.

382 To start, the PSD estimations of AMSR-E LPRM soil moisture product are conducted using
383 the Welch's method with different Hamming window sizes. As stated earlier, the window size
384 determines the amplitude accuracy and frequency resolution of the PSD. To reach a compromise
385 between them and provide sufficient support for detecting periodicity in high frequency, the
386 window size is varied between 270 to 360 days at 10-day intervals. Thus, for each grid, there are
387 ten separate estimates of PSD. These PSDs and corresponding frequency series are then
388 transformed into logarithm space for further analysis. Polynomial interpolation is used to remove
389 the background Brownian shape of PSD, allowing for more accurate detection of the peaks. For
390 detecting the most prominent and consistent 8-day peaks, two thresholds are employed: a) the
391 minimum peak height is no less than 3-sigma (standard deviation) of the de-trended PSD
392 estimations; and b) the 8-day peaks are repeatedly detected by at least 5 times (out of the 10
393 Hamming window sizes considered at each grid). In addition, the same peak detection approach is
394 applied for AMSR-E brightness temperature T_B -derived parameters as described in the following
395 section 2.4.1.

396

397 **2.4. Land Surface Heterogeneity indicator**

398 The land surface characteristics are extremely variable in both space and time. Our strategy
 399 is based on applying the best available global descriptions of land surface characteristics from both
 400 microwave and visible/near-infrared remote sensing and comparing these patterns to maps of 8-
 401 day spectral peak presence. Naturally, all heterogeneity descriptions have resolution limitations
 402 which prevent them from capturing all sub-pixel scale heterogeneity (Lakhankar et al., 2009b).

403 **2.4.1 T_B -derived heterogeneity indicator**

404 The AMSR-E T_B data are re-sampled onto regular quarter degree grid using a drop-in-
 405 bucket approach. Quarter degree grid-scale averages are acquired by averaging all footprints –
 406 across various scans and swath cycles – whose geographic centers fall within a grid box for a given
 407 day. Thereby, the spatial coverage of the effective radiating body can extend beyond the
 408 boundaries of each grid box. In fact, according to Jackson et al. (2010), the main contribution of
 409 radiation can come from a $0.75^\circ \times 0.75^\circ$ box centered at each quarter degree grid. Therefore,
 410 mirroring the land surface parameterization of the LPRM algorithm, a T_B -derived heterogeneity
 411 indicator (TB-HI) is proposed to characterize the spatial heterogeneity of the underlying land
 412 surface (within a centered $0.75^\circ \times 0.75^\circ$ box) for several adjoining satellite footprints within the
 413 same orbital overpass

414
$$H_{3 \times 3}^{TB} = H_{3 \times 3}^{MPDI} + H_{3 \times 3}^{MWE} + H_{3 \times 3}^{TEMP} \quad (7)$$

415 where

416
$$H_{3 \times 3}^{MPDI} = std[\log(MPDI)_{i,j}] \equiv std \left[\log \left(\frac{1}{N} \sum_{t=1}^N \frac{T_{B(V),t}^C - T_{B(H),t}^C}{T_{B(V),t}^C + T_{B(H),t}^C} \right)_{i,j} \right] \quad i, j \sim (1,2,3) \quad (8)$$

417
$$H_{3 \times 3}^{MWE} = std[\log(MWE)_{i,j}] \equiv std \left[\log \left(\frac{1}{N} \sum_{t=1}^N \frac{T_{B(H),t}^C}{T_{B(V),t}^C} \right)_{i,j} \right] \quad i, j \sim (1,2,3) \quad (9)$$

418
$$H_{3 \times 3}^{TEMP} = std \left[\log \left(\frac{1}{N} \sum_{t=1}^N T_{B(V),t}^{Ka} \right)_{i,j} \right] \quad i,j \sim (1,2,3) \quad (10)$$

419 and $std[\sim]$ represents the mathematic operation of calculating standard deviation for a 3×3 box
 420 (i.e., $0.75^\circ \times 0.75^\circ$). In Equations (8–10), i and j are the grid index within the 3×3 box, and N is
 421 the total number of sampled time steps. $H_{3 \times 3}^{MPDI}$ is calculated based on the AMSR-E C-band T_B data
 422 and can be a reflection of both the soil and canopy information (Owe et al., 2001). Moreover, the
 423 effective emissivity ($MWE = T_{B(P)}/T$) is used in Equation 9 to capture the heterogeneity in
 424 emissivity while the Ka-band T_B at V represents the effective surface temperature T . The spatial
 425 variation of temperature is also taken into account using Equation 10. For simplicity, fixed values
 426 of $MPDI$, MWE , and $T_{B(V)}^{Ka}$ are assigned to water bodies: $MPDI = 0.2$ (Chen et al., 2011),
 427 $MWE = 0.5$ (Grody, 1993; Weng, 2010), $T_{B(V)}^{Ka} = 220$ (Lin et al., 1998). The ranges of these
 428 heterogeneity components are slightly different, thus global normalization has been conducted for
 429 each component and $H_{3 \times 3}^{TB}$ (unit-less) is further normalized into $[0,100]$ after arithmetic
 430 summation. Note that this heterogeneity indicator is computed directly from the AMSR-E
 431 observed T_B data without any other auxiliary biophysical information sources and can be adapted
 432 to other microwave satellite or retrieval algorithms as well. For example, C-band $T_{B(P)}^C$ could be
 433 replaced with L-band $T_{B(P)}^L$ acquired from the SMOS and SMAP missions, while surface
 434 temperature data could also potentially be derived from land surface model output.

435 *2.4.2 NDVI-derived heterogeneity indicator*

436 Vegetation canopy plays an important role in observing and retrieving soil moisture from
 437 space-borne platforms (Jackson et al., 1982). NDVI is a simple index of vegetation density which
 438 can be applied for depicting the land surface characteristics. To take into account the canopy, a

439 straightforward NDVI-derived heterogeneity indicator (VI-HI) is proposed with a form similar to
 440 TB-HI

$$441 \quad H_{3 \times 3}^{VI} = std \left[\left(\frac{1}{N} \sum_{t=1}^N NDVI_t \right)_{i,j} \right] \quad i, j \sim (1, 2, 3) \quad (11)$$

442 where the standard deviation ($std[\sim]$) of NDVI is calculated for a 3×3 box centered at each
 443 quarter degree grid. This indicator characterizes the spatial variability of vegetation density over
 444 the average main-beam FOV of AMSR-E.

445 2.4.3 Land cover-derived heterogeneity indicator

446 Different land cover types can demonstrate distinct physical characteristics with varying
 447 temporal climatology. Regions with various land cover types can be quite heterogeneous with
 448 regard to satellite-based soil moisture retrieval. Therefore, a land cover-derived heterogeneity
 449 indicator (LC-HI) is defined as the number of individual land cover types contained within a single
 450 $0.75^\circ \times 0.75^\circ$ box for each quarter degree grid

$$451 \quad H_{3 \times 3}^{LC} = |(\langle LC_k^{Perc} \geq 10 \rangle \cup \langle 10 > LC_{Water}^{Perc} > 0 \rangle)_{i,j}| \quad k \sim (1, 9) \quad i, j \sim (1, 2, 3) \quad (12)$$

452 where $|\sim|$ denotes the cardinality operator, LC_k^{Perc} represents the grid area in percent classified as
 453 land cover type k (out of nine classes), and LC_{Water}^{Perc} is the percentage classified as Water. Open
 454 water, with its high dielectric constant, has a profound impact on the microwave emission and even
 455 small fractions of open water may greatly alter the T_B observations (Loew, 2008). In this case, LC-
 456 HI will increase 1 if there is open water within the 3×3 box. The other land cover classes are only
 457 taken into account when their percentages are larger than 10%.

458

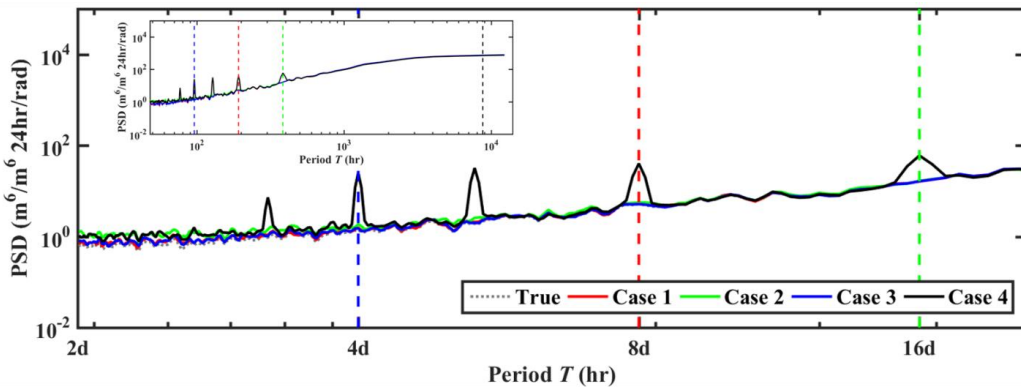
459 **III. Results**

460 Our main interest is examining the most prominent and consistent spectral peaks generated
 461 from AMSR-E's periodic sampling pattern and the relationship between these peaks and the

462 spatial heterogeneity of the corresponding land surface. To physically explore the occurrence of
 463 high frequency spectral peaks, both the synthetic experiment and a detailed site-specified analysis
 464 are discussed first. Subsequently, the global distribution of the 8-day periodic errors, and their
 465 relationship with the spatial heterogeneity indicators introduced in section 2.4, is presented.

466 *3.1 Synthetic experiments*

467 Figure 5 demonstrates the PSD estimations of five synthetic soil moisture time series (as
 468 described in section 2.3.3). Compared to the “True” scenario, both Case 1 and Case 3 show quite
 469 similar spectral characteristics suggesting that the land cover heterogeneity alone cannot lead to
 470 high-frequency peaks without periodic sampling pattern. While both Case 2 and Case 4 exhibit a
 471 moderate noise floor over the “True” soil moisture for periods between 2- and 4-days. Particularly,
 472 significant frequency peaks are exposed when the periodic sampling pattern is combined with
 473 spatial heterogeneity in Case 4. The results suggest that, in the absence of either the spatial
 474 heterogeneity or periodic sampling patterns, high frequency peaks cannot be produced.



475
 476 **Figure 5.** High-frequency PSD for soil moisture time series generated by the synthetic “True” case and the synthetic
 477 “satellite-based” Cases 1–4. The Hamming window size is set equal to 365 days. The entire PSDs (including lower-
 478 frequency components) are shown in the upper left corner. From left to right, the colored dashed vertical lines represent
 479 4-day, 8-day, 16-day, and 365-day periods. Note that the PSDs of the ‘True’ case and Cases 1–3 are virtually
 480 indistinguishable.

481 Additionally, the influence of different re-gridding methods on the occurrence of spectral
482 peaks has been explored. All PSD estimations of three re-gridded soil moisture time series have
483 shown notable spectral peaks, indicating that the peaks are result for a combination of periodic
484 sampling patterns and stable spatial heterogeneity – regardless of exact re-gridding method applied
485 (see section B of the supporting materials for further discussion).

486 **3.2. Site-specified analysis**

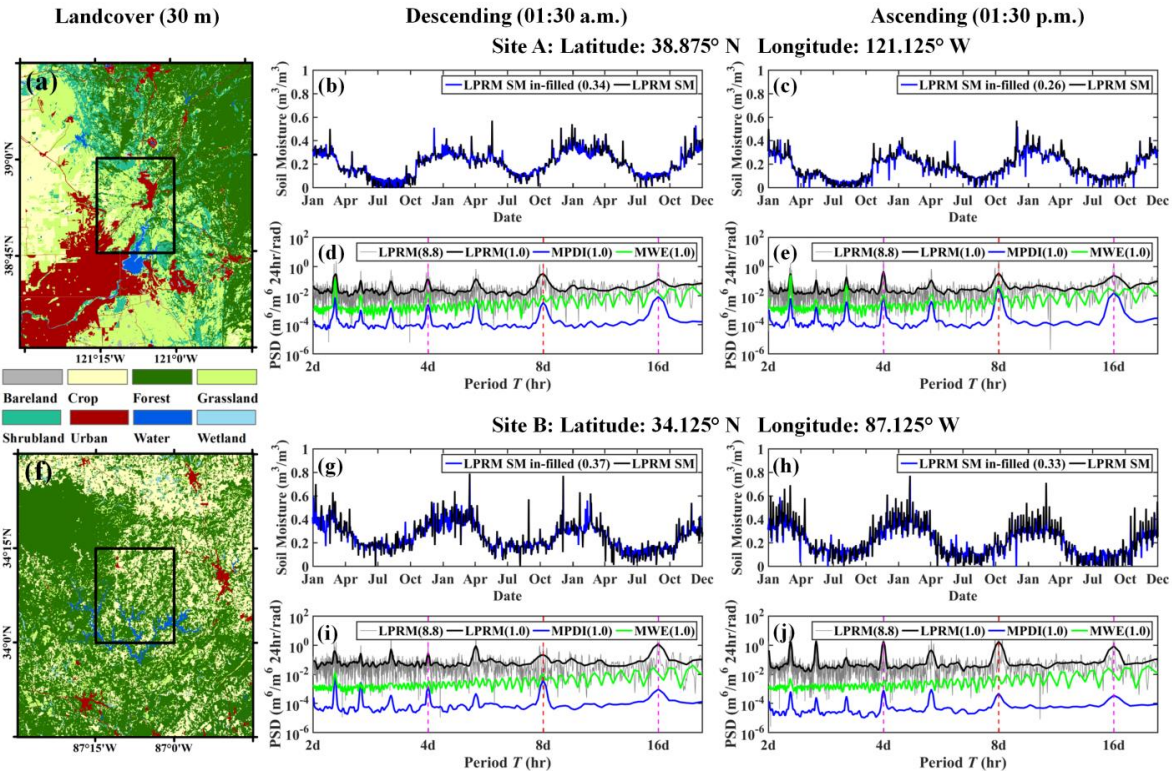
487 Figure 6.a and 6.f show land cover maps for two arbitrary $0.75^\circ \times 0.75^\circ$ grids within North
488 America (hereafter referred as to Sites A and B). Also shown are the enlarged 3-year time series
489 (from January 2004 to December 2006) for AMSR-E LPRM soil moisture and corresponding
490 spectral analysis within each $0.25^\circ \times 0.25^\circ$ grid located at the center of these $0.75^\circ \times 0.75^\circ$ grids –
491 as outlined by the black boxes. Both sites in Figure 6 represent highly heterogeneous land surface
492 conditions. From the GlobeLand30 land cover map of Site A (latitude: 38.875° N, longitude:
493 121.125° W), a highly heterogeneous satellite orbit overpassing region can be observed with large
494 portions of forest and urban land cover. Meanwhile, the fractions of water bodies, crop, grassland,
495 and shrubland land cover types are also non-trivial with a relatively clear spatial pattern (Figure
496 6.a). In particular, the urban area is mainly located in the lower-left corner, while forest covers
497 upper-right corner. Grassland is mixed with crop, shrubland and water bodies. A strong negative
498 trend in vegetation density from upper-right to lower-left can be observed.

499 The soil moisture time series for Site A (Figure 6.b and Figure 6.c) demonstrates a
500 relatively strong seasonal climatology with values varying from 0.01 to 0.5 (m^3/m^3). AMSR-E
501 LPRM soil moisture retrieval for each quarter degree grid is generated based as the mean of all
502 swath data whose footprint centers fall within that particular grid (Owe et al., 2008). The soil
503 moisture record manifests several significant spectral resonances – including a significant 8-day

504 peak. Moreover, 4-day and 16-day peaks are also conspicuous for both overpasses. Given their
505 uses in LPRM retrievals, the T_B -derived *MPDI* and *MWE* are also analyzed in frequency domain.
506 Similarly, an 8-day peak in *MPDI* appears in both half-orbits – suggesting that the spectral peaks
507 in soil moisture retrievals can be traced back to the *MPDI*. However, the probability of occurrence
508 and the relative amplitude of spectral peaks in soil moisture and *MPDI* are not exactly the same
509 for each peak. On the other hand, the PSDs of *MWE* also show 8-day and 4-day spectral peaks for
510 the ascending overpass (Figure 6.e) and a 4-day peak for the descending overpass (Figure 6.d).
511 Therefore, within Site A, strong spatial heterogeneity in land cover appears capable of generating
512 soil moisture spectral peaks associated with the satellite orbiting cycle.

513 Likewise, Site B (latitude: 34.125° N, longitude: 87.125° W) exhibits strong spatial land
514 cover heterogeneity (Figure 6.f). Specifically, forest covers the north-western regions and is mixed
515 with crops and grasslands. Small patches of urban and water bodies are sparsely distributed
516 throughout the scene. The soil moisture time series values range from 0.01 to 0.7 (m^3/m^3). Despite
517 a lack of strong large-scale spatial variation, this site also demonstrates heterogeneous land surface
518 characteristics with different land cover types thoroughly mixed with each other. Both the
519 ascending and descending soil moisture time series contain 8-day peaks in the frequency domain
520 (Figure 6.i and Figure 6.j) with the ascending peak more prominent. For the descending overpass,
521 the more equivalent thermodynamic conditions are beneficial for applying the LPRM soil moisture
522 retrieval algorithm. A significant 8-day peak in the descending *MPDI* does not lead to a
523 comparable peak in the soil moisture retrievals (Figure 6.i). Also, fewer peaks are observed in the
524 PSDs of *MWE* compared to Site A. Other factors such as the vegetation density and soil and canopy
525 effective temperatures in the retrieval process can play a role in determining the retrieved soil
526 moisture. Specifically, the microwave radiation emitted from water bodies is quite different from

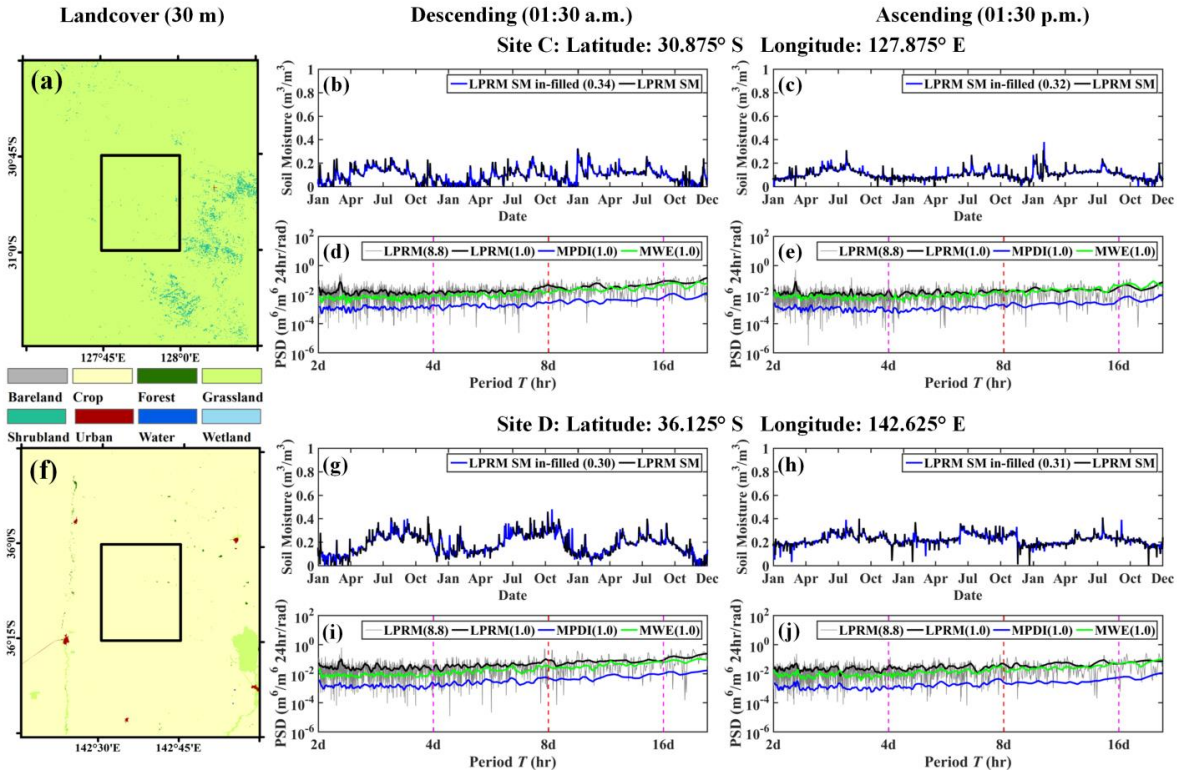
527 other land cover types and can strongly impact in soil moisture retrievals (Gouweleeuw et al.,
 528 2012).



529
 530 **Figure 6.** Site-specified demonstrations of high resolution land cover (a and f), descending (b, d, g, and i) and
 531 ascending (c, e, h, and j) AMSR-E LPRM soil moisture and brightness temperature (T_B). Each land cover map depicts
 532 a $0.75^\circ \times 0.75^\circ$ grid centered at different locations (Sites A and B) with the black box outlines the $0.25^\circ \times 0.25^\circ$ grid.
 533 Maps are projected in WGS 1984 UTM coordinate system and latitudes and longitudes of sites are shown as well.
 534 Enlargements of the 3-years (from January 2004 to December 2006) time series of soil moisture retrievals are included
 535 for each site and the infilling fractions are shown in the brackets. The spectral analyses are conducted for AMSR-E
 536 LPRM soil moisture retrievals and T_B -derived Microwave Polarization Difference Index (*MPDI*) and Microwave
 537 Emissivity (*MWE*). The Hamming window sizes for PSD estimations are indicated by units of year in the brackets.
 538 Dotted vertical lines represent three periods at 4-day, 8-day, and 16-day.

539 In contrast to the relatively heterogeneous sites examined in Figure 6, Figure 7 looks at two
 540 spatially homogeneous sites (Sites C and D). The two sites are dominated by grassland and crop
 541 cover, respectively. The coverage fractions of other land cover types are relatively negligible. Both

542 soil moisture time series depict a relatively small seasonal climatology compared to Figure 6
 543 without the orbiting cycle-related spectral peaks. Also, no prominent peaks are observed from the
 544 PSDs of both T_B -derived $MPDI$ and MWE .



545
 546 **Figure 7.** Same with Figure 6 except for Sites C and D.

547 By investigating four different sites with various spatial coverages of land cover types, a
 548 possible link between spectral peaks of retrieved soil moisture and the directly observed T_B can be
 549 inferred. The spatial heterogeneity combined with systematic orbiting cycle can lead to the spectral
 550 peaks in $MPDI$ and thus soil moisture retrievals.

551
 552 **3.3. Global distribution of spectral peaks**

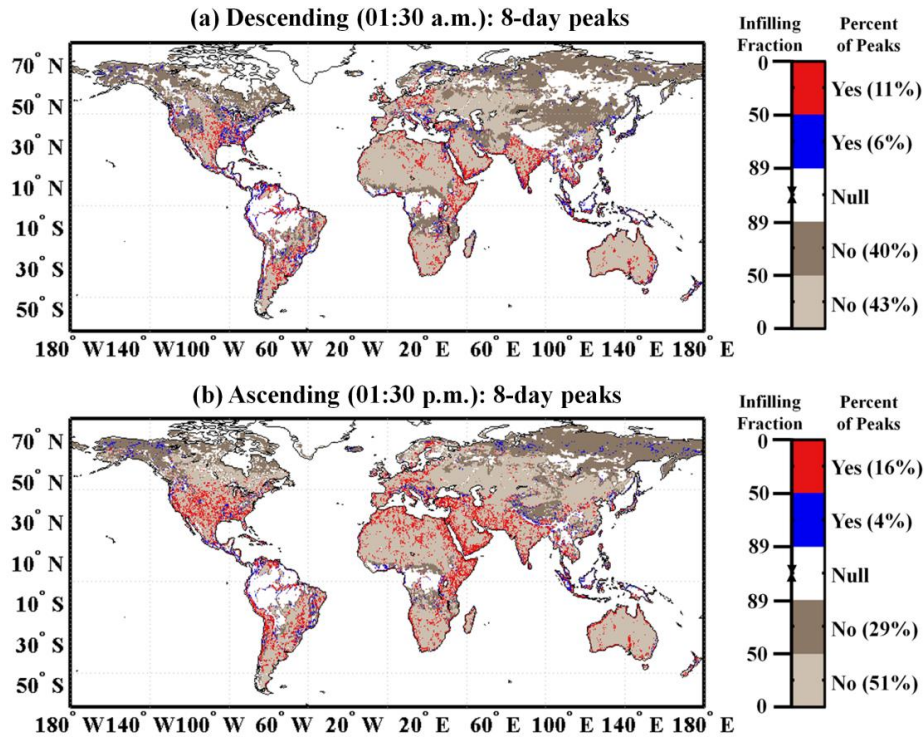
553 While interesting, results in Figures 6 and 7 are clearly anecdotal in nature. In order to
 554 examine more general tendencies, global distributions of the 8-day spectral peaks in LPRM
 555 AMSR-E soil moisture retrievals are plotted in Figure 8 for both descending and ascending

556 overpasses. Regions with high (over 50%) infilling fractions (Figure 1.c and 1.d) are indicated
557 with different color settings for grids with or without 8-day spectral peaks.

558 Generally speaking, the spatial distribution of spectral peaks is similar for both half-orbits.
559 However, relatively more peaks are found in the ascending half-orbit – 20% versus 17% of the
560 total grids over the globe. Both descending and ascending overpasses have demonstrated notable
561 spectral peaks over densely-vegetated areas of Eastern CONUS. On the other hand, there exist
562 moderately different distributions of peaks over Western CONUS. Note that significant
563 discrepancies of near-surface (soil, canopy and air) vertically thermal profiles can be observed
564 between the AMSR-E nighttime descending (01:30 a.m.) and daytime ascending (01:30 p.m.)
565 overpasses. During nighttime, near-surface isothermal conditions benefit the retrieval of soil
566 moisture from brightness temperature observations with higher accuracy (Jackson et al., 2010),
567 yielding less spurious spectral peaks in the descending overpass.

568 Comparing regions with high infilling fractions (blue and dark brown in Figure 8) against
569 other grids (red and light brown), the probability of identified peaks can be lower with 12% (4/33)
570 versus 24%, and 13% versus 20% for ascending and descending overpasses, respectively. With
571 increased infilling fractions, more in-filled data are included for the peak detection, which may
572 lead to possible missed identification of peaks (please refer to section A of the supporting materials
573 for more details). Nevertheless, as our gap-filling approach does not lead to occurrence of peaks,
574 any peaks detected for grids with high infilling fraction should be prominent and therefore are
575 preserved for the global distribution mapping.

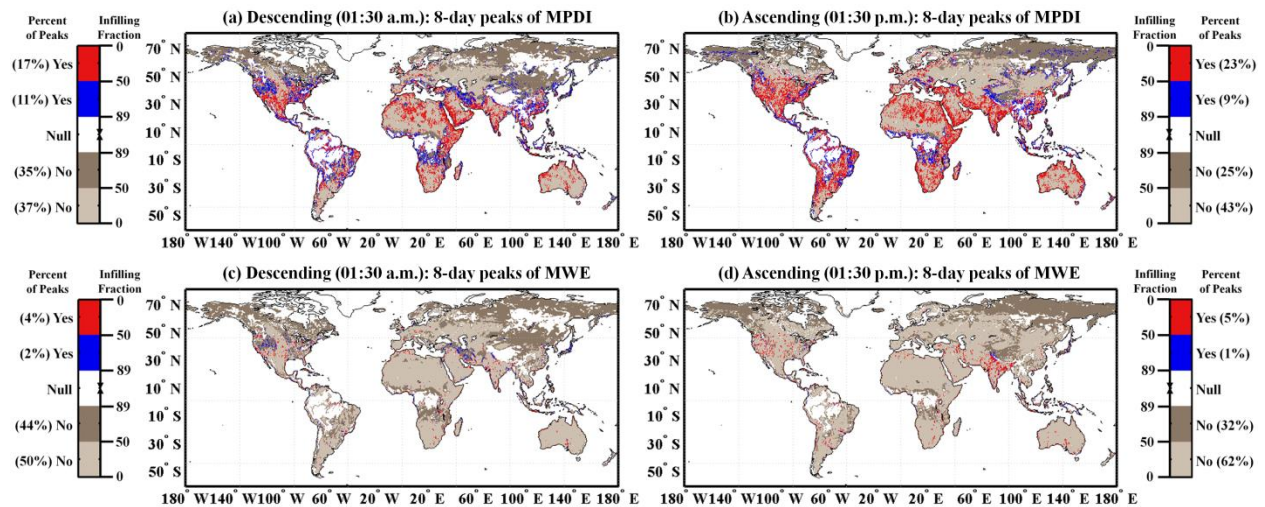
576 Additionally, comparing Figure 8 and Figure 1.a or Figure 1.b, the presence of RFI may
577 impact the occurrence of spectral peaks. See section 4.1 for additional discussion on this point.



578

579 **Figure 8.** Global distribution maps of 8-day spectral peaks in the AMSR-E LPRM soil moisture product for both (a)
 580 descending and (b) ascending half-orbits. Regions with in-filled data over (below) 50% are shown in dark (light)
 581 brown. Accordingly, grids with peaks are demonstrated in blue or red color. Percentages of grids with/without 8-day
 582 peaks in regard to the total grids for both descending and ascending overpasses are computed, respectively.

583 Furthermore, the global spectral analyses are conducted for the T_B -derived *MPDI* and
 584 *MWE* as shown in Figure 9. As depicted, both descending (Figure 9.a and 9.c) and ascending
 585 (Figure 9.b and 9.d) half-orbits have a similar spatial distribution pattern with regard to *MPDI* or
 586 *MWE*. Overall spatial patterns of 8-day peaks in *MPDI* are comparable with that in soil moisture
 587 retrievals. However, 8-day peaks in *MPDI* are relatively more common than soil moisture peaks
 588 in Figure 8. Comparing to (relatively dynamic) soil moisture values, *MPDI* is more likely to
 589 respond to temporally-stable land surface elements, such as land cover type and vegetation density.



590

591 **Figure 9.** Global distribution maps of 8-day spectral peaks in AMSR-E -derived *MPDI* (a and b) and *MWE* (c and d)
 592 for both descending and ascending half-orbits. Color setting is same as Figure 8 and percentages of grids with/without
 593 8-day peaks are also shown in the legend.

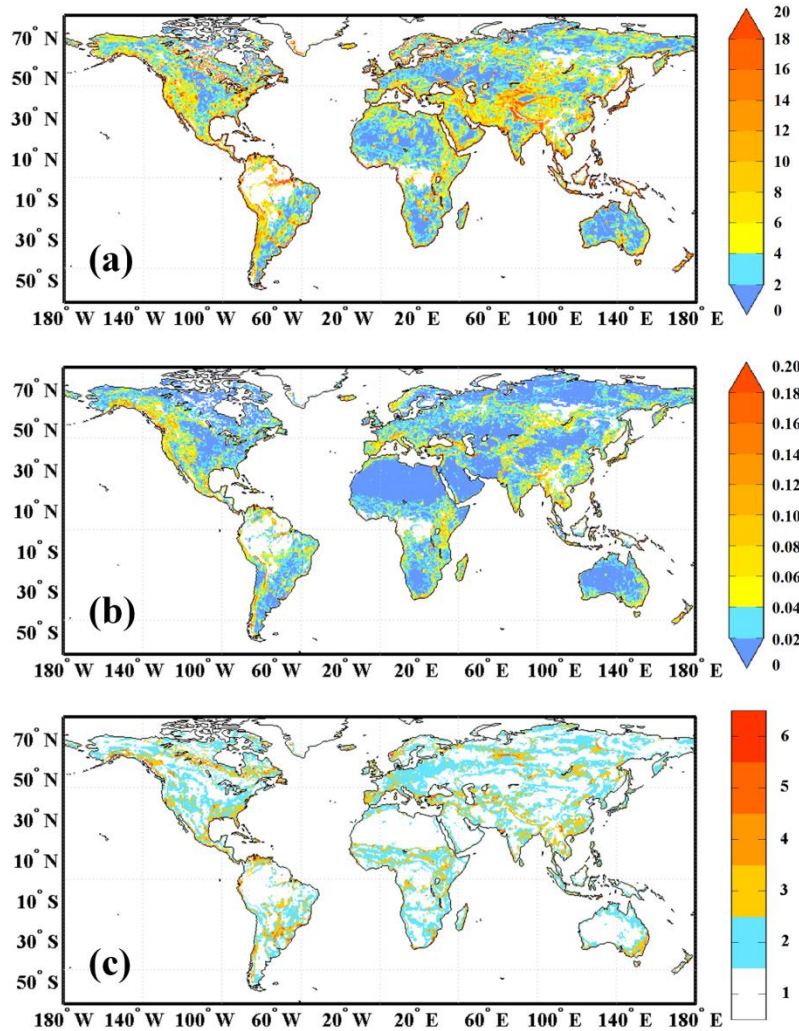
594 In contrast, *MWE* maps demonstrate relatively fewer peaks than soil moisture in Figure 8.
 595 *MWE* as a function of several varying variables, including water content and soil salinity, changes
 596 rapidly over land surface (Prigent et al., 2006). More specifically, the intensity and duration of
 597 precipitation events modulate the land surface emissivity (Ferraro et al., 2013). Consequently,
 598 *MWE* does not generally show strong and persistent land surface heterogeneity over the 16-day
 599 exact repeat cycle of AMSR-E sensor. Taken as a whole, Figure 9 suggests a primary role for
 600 *MPDI* as the source of periodicity in LPRM soil moisture retrievals.

601

602 **3.4. Relating the 8-day periodic error to spatial heterogeneity**

603 To explore the relationship between the presence of an 8-day spectral peak in soil moisture
 604 retrievals and the land surface spatial heterogeneity, three heterogeneity indicators are computed
 605 for each quarter degree grid (see section 2.4 above). Figure 10 shows global maps of these three
 606 heterogeneity indicators, namely TB-HI, VI-HI, and LC-HI. For each map, larger values indicate

607 larger amounts of land surface spatial heterogeneity although the valid ranges are different for each
608 indicator (see Table 1 for details).



609
610 **Figure 10.** Global maps of three heterogeneity indicators calculated from: (a) AMSR-E T_B observations, (b) long-
611 term averaged vegetation index and (c) land cover types.

612 The three maps show different aspects of spatial heterogeneity which results in different
613 distributions of indicator values. Nevertheless, the spatial distribution of high heterogeneity
614 indicators is generally consistent with the occurrence of 8-day peaks in the AMSR-E LPRM soil
615 moisture product (Figure 8). Regions such as the Amazon and the Tibetan Plateau have
616 demonstrated a significant relationship that grids with 8-day peaks have extremely high TB-HI

617 (Figure 10.a). Likewise, in western CONUS, South America, South Africa, and India, a relatively
618 close link can be observed. Along the west coast of South America and over West Central Africa,
619 a comparable distribution of high VI-HI and grids with 8-day peak is observable (Figure 10.b).
620 LC-HI also shows some high values for central Southern Africa (Figure 10.c) where 8-day peaks
621 are frequently detected.

622 Both VI-HI and LC-HI fail to capture the information over non-vegetated landscapes, e.g.,
623 North Africa and the Arabian Peninsula. These two indicators are based solely on relatively coarse-
624 resolution land cover characteristics and cannot fully represent the land surface variability. Instead,
625 other factors not captured in the indices, such as soil texture and roughness, may play a primary
626 role in determining the heterogeneity for low-vegetated regions.

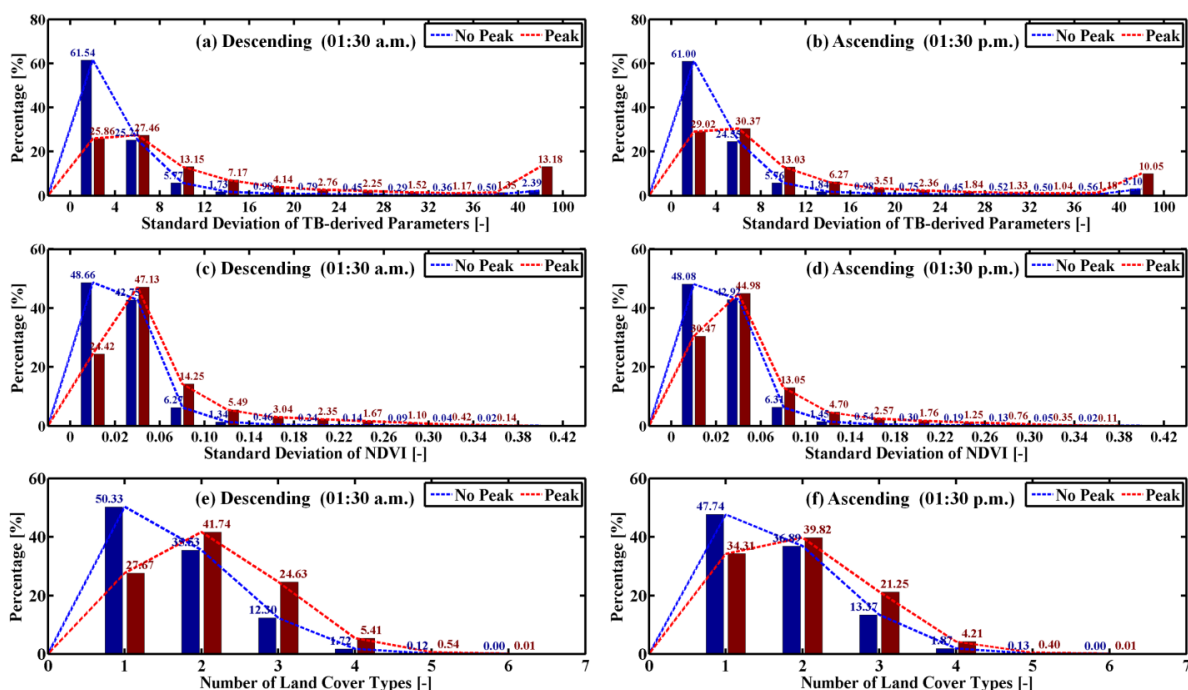
627 Table 1 shows the global mean and median values for each of the three indicators, both for
628 grids with and without 8-day peaks. Under all circumstances, grids with the 8-day peak are
629 associated with relative higher mean and median values of the heterogeneity indicators. This
630 further suggests that the occurrence of spectral peaks can be related to the land surface spatial
631 heterogeneity. In addition, Figure 11 shows the normalized histograms (to [0,100]) of three
632 indicators over the globe for grids with or without 8-day peaks. Descending and ascending
633 overpasses are separately processed and the statistical hypothesis test (Wilcoxon-Mann-Whitney
634 test) has been performed for six scenarios. All test results indicate that the median of the indicator
635 for grids with peaks is greater than that for grids without peaks at a 0.001 significance level. This
636 suggests a statistically significant capability for the three heterogeneity indicators to characterize
637 regions with strong land surface variability.

638 **Table 1.** Global means and medians of three heterogeneity indicators under two conditions: with or without 8-day
639 peaks identified in soil moisture retrievals. Statistics for both descending (01:30 a.m.) and ascending (01:30 p.m.)
640 half-orbits are calculated. Data in parentheses are computed for regions with infilling fraction smaller than 50%.

Indicator	Descending		Ascending		Valid Range
	Yes	No	Yes	No	
Mean					
TB-HI	15.30 (13.01)	5.70 (4.89)	12.98 (11.45)	6.18 (4.91)	[0 100]
VI-HI	0.06 (0.05)	0.03 (0.03)	0.05 (0.05)	0.03 (0.03)	[0 0.4]
LC-HI	2.09 (2.07)	1.66 (1.62)	1.97 (1.94)	1.70 (1.63)	[1 6]
Median					
TB-HI	7.29 (6.91)	3.20 (3.09)	6.38 (6.21)	3.22 (3.01)	[0 100]
VI-HI	0.04 (0.04)	0.02 (0.02)	0.03 (0.03)	0.02 (0.02)	[0 0.4]
LC-HI	2 (2)	1 (1)	2 (2)	2 (1)	[1 6]

641

642 For grid cells without peaks, nearly half has the lowest level of spatial heterogeneity
643 indicators. For example, 61.54% (61.00%) of grids without peaks in descending (ascending)
644 overpass has a TB-HI smaller than 4 (Figure 11.a and 11.b). Conversely, over 74% (71%) of grids
645 with peaks in descending (ascending) overpass has a TB-HI larger than 4. Similar contrasts can be
646 found for the other indicators. Overall, grids with higher values of the heterogeneity indicators are
647 more likely to contain 8-day peaks in soil moisture retrievals.



648

649 **Figure 11.** Histograms of three heterogeneity indicators for grids with or without 8-day peaks. Descending and
650 ascending overpasses are separately processed over the globe.

651

652 **IV. Discussion**

653 The accurate characterization of errors in remotely sensed soil moisture products is
654 important for satellite calibration/validation activities and the development of optimized
655 assimilation approach for integrating retrievals with hydrologic modeling. In contrast to the
656 common assumption of temporally white errors, Su et al. (2013a) demonstrated that AMSR-E and
657 SMOS gridded soil moisture products over Australia depict spectral resonances suggesting the
658 existence of periodic errors. Here, we expanded the time series spectral analysis in Su et al. (2013a)
659 to a global domain and explored the physical origins of these periodic errors.

660 Through the synthetic experiments, the periodic errors can be linked to the combination of
661 the periodic sampling patterns and the land surface spatial heterogeneity (Figure 5). Results of
662 AMSR-E LPRM soil moisture product further presented a link of spectral peaks existing in T_B -
663 derived *MPDI* and soil moisture retrievals. More specifically, that spatial heterogeneity within the
664 satellite's field-of-view can lead to the periodicity in *MPDI* estimates which are then transmitted
665 into soil moisture retrievals. As demonstrated in Figure 8, LPRM soil moisture derived from both
666 ascending and descending overpasses demonstrate significant 8-day spectral peaks along coastal
667 areas and some regions with water bodies, e.g., the Amazon floodplain and areas of central
668 Australia with ephemeral salt lakes. In addition, regions with spatially-heterogeneous land cover
669 (e.g., eastern CONUS, South America, Western Europe, Peninsular India, and southern China)
670 appear more likely to have the 8-day peaks.

671

672 *4.1. Potential role of radio frequency interference*

673 The AMSR-E LPRM soil moisture product is a combined product which has utilized both
674 C- and X-band T_B to retrieve soil moisture. The C-band frequency, which is theoretically more
675 sensitive to variations in soil moisture, is treated as the primary data source. However, over regions
676 with high RFI contaminations, the retrieval method switches from C- to X-band (shown in Figure
677 1.a and 1.b). This strategy can largely mitigate the influence of strong and spatio-temporally
678 constant RFI. Figure 6 shows an illustration of RFI impact at two heterogeneous sites with
679 contrasting land surface characteristics. For Site A, urban area covers a large portion of the
680 $0.75^\circ \times 0.75^\circ$ grid and only X-band T_B has been utilized for retrieving soil moisture. While the RFI
681 impact has been eliminated to a great extent, spectral peaks are detected from the corresponding
682 soil moisture retrievals (Figure 6.d and 6.e). In contrast, without significant RFI at Site B, C-band
683 T_B has been applied and periodic errors still exist (as shown in Figure 6.i and 6.j). This suggests
684 that the periodicity found in AMSR-E LPRM soil moisture product cannot be fully attributed to
685 RFI alone.

686 On the other hand, in addition to the T_B -derived heterogeneity indicators, another two
687 indicators which are computed from independent MODIS vegetation index and land cover type
688 information will not reflect RFI information. As depicted in Figure 11, VI-HI and LC-HI have
689 demonstrated statistically significant skills in characterizing land surface heterogeneity. Via a pre-
690 defined threshold for each heterogeneity indicator, VI-HI and LC-HI can partially differentiate
691 grids with peaks from those without peaks indicating the causal relationship between spatial
692 variability of natural land surface and the occurrence of peaks.

693 Nevertheless, similarities between RFI map (Figure 7.a in Njoku et al., 2005) and
694 ascending spectral peak map (Figure 8.b) can be observed, for example over CONUS and the

695 western Arabian Peninsula. Note that the RFI detection method is based on the spectral difference
696 between the 6.9- and 10.7 GHz channels and a threshold should be assigned to determine whether
697 RFI exists or not (Li et al., 2004). Consequently, if RFI is of low-level or spatially/temporally
698 intermittent (which is often the real case), it might escape the detection. Moreover, regions with
699 RFI contaminations are often close to urban areas, where transitions in architecture and building
700 density, vegetation, and anthropogenic activity are thoroughly mixed (Cadenasso et al., 2007).
701 Under such circumstance, a high heterogeneity of land surface characteristics (including both
702 natural and artificial features) can be observed over these regions and thus lead to more spectral
703 peaks in soil moisture retrievals. Therefore, RFI can intensify the land surface heterogeneity and
704 increase the probability of occurrence of spectral peaks in satellite-derived soil moisture retrievals.

705

706 ***4.2. Impact of the infilling method***

707 To conduct the spectral analysis, the 1-D infilling method was performed to achieve
708 evenly-spaced observations. Given that the infilling method is based on statistics sampled from
709 the entire time series, the results retain the autocorrelation structure of soil moisture in the high
710 frequency domain but in-filled values are smoothed with low frequency climatology for significant
711 gaps (Wang et al., 2012). Comparing Figure 1.c or 1.d with Figure 8, no obvious spatial correlation
712 between the infilling fraction and existence of 8-day peak can be observed – suggesting that our
713 infilling approach does not lead to the spurious production of spectral peaks. Aside from high
714 latitudes near the pole where the interpolation fraction is extremely large and there is less chance
715 of having 8-day peaks, in most regions with small infilling fractions, such as Western Europe,
716 South America, Africa, and Australia, there is no evidence that the gap infilling has an impact on
717 the frequency of peak occurrence.

718 In order to further examine this point, a synthetic control test has been conducted to explore
719 the impact of infilling fraction. Details can refer to section A in the supporting materials. The
720 results demonstrated that, as expected, the accuracy of in-filled soil moisture time series gradually
721 decreases with increasing infilling fractions. However, no spurious spectral peaks will be
722 introduced by the infilling method, suggesting that any spectral peaks detected in the in-filled soil
723 moisture data are present in the original time series. Further studies may explore alternative PSD
724 estimation approaches (such as the Lomb-Scargle periodogram (Lomb, 1976; Scargl, 1982) or
725 wavelet transform-based method (Foster, 1996) which do not require evenly-spaced observations.

726

727 ***4.3. Potential applications***

728 Results in Figure 8 identified significant periodic error components in existing soil
729 moisture remote sensing product and globally mapped their distribution. Removing such
730 systematic error components is a critical goal of satellite calibration activities and could potentially
731 aid in the development of optimized gridding and processing procedures. A global identification
732 map of such periodic errors would also be beneficial for identifying highly heterogeneous regions
733 for the targeted application of a band-stop filter (Su et al., 2013a; 2015) for removing the
734 systematic periodic errors in short-term satellite-derived soil moisture products.

735 For short-term available satellite-based soil moisture products, the baseline of applying the
736 band-stop filtering is to apply it indiscriminately to every grid cell. In this case, the majority of
737 grids without significant frequency peaks can be over-smoothed (because over 80% of global grid
738 cells lack 8-day soil moisture peaks). Moreover, spatial heterogeneity may similarly affect other
739 satellite-based products, particularly when they have similar orbital configurations and retrieval
740 inputs as AMSR-E LPRM. For satellite records which are too short for PSD estimation, one option

741 is to utilize a peak distribution map generated from the long-term (9+ year) AMSR-E soil moisture
742 time series as the criterion for identifying heterogeneous regions in which to apply a band-stop
743 filter.

744

745 **V. Conclusions**

746 Via a synthetic experiment imitating the periodic sampling pattern of polar-orbiting
747 satellite swaths over various land cover characteristics, the combination of spatial land surface
748 heterogeneity and periodic orbital sampling pattern are linked to periodic errors in remotely-sensed
749 soil moisture retrievals (Figure 5). In data real cases utilizing AMSR-E LPRM soil moisture
750 retrievals, site-specific studies demonstrate that the satellite repeat cycle can generate a periodicity
751 in the T_B -derived *MPDI* and corresponding LPRM soil moisture retrievals (Figures 6 and 7). By
752 applying the peak detection method, global distribution maps of 8-day peaks in AMSR-E LPRM
753 soil moisture retrievals and T_B -derived *MPDI* and *MWE* can be generated. Comparisons between
754 these maps show strong evidence that the satellite orbiting cycle-related spectral peaks are more
755 likely to occur in highly-heterogeneous land regions (Figures 8 and 9). The conclusion is intuitive
756 to understand. The re-gridding method of satellite observations is usually based on a selection of
757 all footprints within the same orbital overpass covering the given grid. Due to the progression of
758 the satellite orbit, the track changes from day to day with an exact repeat cycle and thus introduces
759 the periodic errors into the sampling over regions with large land surface heterogeneity.

760 The global identification of the periodic error is of importance for the data assimilation
761 community and will also support the development of improved soil moisture re-gridding and post-
762 processing methods. To globally correlate the occurrence of such spectral peaks with heterogeneity
763 in land surface characteristics, three heterogeneity indicators have been proposed and shown their

764 statistically significant capability in detecting high-heterogeneous regions with 8-day peaks
765 (Figure 10, Figure 11, and Table 1). The association between heterogeneity indicators and the
766 occurrence of 8-day periodic errors is compelling evidence of the causal link between land surface
767 spatial heterogeneity and the periodic errors in satellite-based re-gridded soil moisture product.

768 While these heterogeneity indicators have demonstrated statistically significant skills at a
769 global scale, they do not predict all peaks (and predict some peaks which do not occur). As a result,
770 further refinement of these indicators is necessary to make them of immediate value in an
771 operational retrieval and/or data assimilation context. Nevertheless, results presented here
772 represent an important first step in this direction as both synthetic and real data results provide
773 clear evidence of a general link between land surface spatial heterogeneity and the occurrence of
774 periodic errors in AMSR-E soil moisture retrievals. Additionally, other PSD estimation approaches
775 and soil moisture products using different retrieval algorithms (Kim et al., 2015), such as the JAXA
776 product retrieved by Japan Aerospace Exploration Agency, should be included in follow-on
777 analyses.

778

779 **Acknowledgement**

780 The authors would like to acknowledge the contribution of Land Parameter Retrieval
781 Model development team, all scientists that provided their ground-based measurements with the
782 International Soil Moisture Network, the GlobeLand30 research group for sharing the high
783 resolution land cover data, the MODIS science team for providing accessible data products. The
784 authors would also like to thank the four anonymous reviewers for their constructive comments.
785 This work was supported by the Cross-disciplinary Collaborative Teams Program for Science,
786 Technology and Innovation of the Chinese Academy of Sciences.

788 **References**

- 789 Al-Yaari, A., J. P. Wigneron, A. Ducharne, Y. Kerr, P. De Rosnay, R. De Jeu, A. Govind, A. Al Bitar, C. Albergel,
790 and J. Munoz-Sabater (2014), Global-scale evaluation of two satellite-based passive microwave soil moisture
791 datasets (SMOS and AMSR-E) with respect to Land Data Assimilation System estimates, *Remote Sensing of*
792 *Environment*, 149, 181-195.
- 793 Alvarez-Garreton, C., D. Ryu, A. Western, W. Crow, and D. Robertson (2014), The impacts of assimilating satellite
794 soil moisture into a rainfall–runoff model in a semi-arid catchment, *Journal of Hydrology*, 519, 2763-2774.
- 795 Bolten, J. D., W. T. Crow, X. Zhan, T. J. Jackson, and C. A. Reynolds (2010), Evaluating the utility of remotely sensed
796 soil moisture retrievals for operational agricultural drought monitoring, *IEEE Journal of Selected Topics in*
797 *Applied Earth Observations and Remote Sensing*, 3(1), 57-66.
- 798 Brocca, L., S. Hasenauer, T. Lacava, F. Melone, T. Moramarco, W. Wagner, W. Dorigo, P. Matgen, J. Martínez-
799 Fernández, and P. Llorens (2011), Soil moisture estimation through ASCAT and AMSR-E sensors: An
800 intercomparison and validation study across Europe, *Remote Sensing of Environment*, 115(12), 3390-3408.
- 801 Brovelli, M. A., M. E. Molinari, E. Hussein, J. Chen, and R. Li (2015), The first comprehensive accuracy assessment
802 of GlobeLand30 at a national level: methodology and results, *Remote Sensing*, 7(4), 4191-4212.
- 803 Burgers, G., P. Jan van Leeuwen, and G. Evensen (1998), Analysis scheme in the ensemble Kalman filter, *Monthly*
804 *Weather Review*, 126(6), 1719-1724.
- 805 Cadenasso, M. L., S. T. Pickett, and K. Schwarz (2007), Spatial heterogeneity in urban ecosystems: reconceptualizing
806 land cover and a framework for classification. *Frontiers in Ecology and the Environment*, 5(2), 80-88.
- 807 Chan, S., E. Njoku, and A. Colliander (2012), SMAP Algorithm Theoretical Basis Document: L1C Radiometer Data
808 Product, Tech. Rep. SMAP Project, JPL D-53053, Jet Propulsion Laboratory, Pasadena, CA.
- 809 Chen, J., J. Chen, A. Liao, X. Cao, L. Chen, X. Chen, C. He, G. Han, S. Peng, and M. Lu (2015), Global land cover
810 mapping at 30m resolution: A POK-based operational approach, *ISPRS Journal of Photogrammetry and Remote*
811 *Sensing*, 103, 7-27.
- 812 Chen, S. S., X. Z. Chen, W. Q. Chen, Y. X. Su, and D. Li (2011), A simple retrieval method of land surface temperature
813 from AMSR-E passive microwave data—A case study over Southern China during the strong snow disaster of
814 2008. *International Journal of Applied Earth Observation and Geoinformation*, 13(1), 140-151.
- 815 Crow, W. T., and M. Van den Berg (2010), An improved approach for estimating observation and model error
816 parameters in soil moisture data assimilation, *Water Resources Research*, 46(12), W12519.
- 817 Crow, W. T., and X. Zhan (2007), Continental-scale evaluation of remotely sensed soil moisture products, *IEEE*
818 *Geoscience and Remote Sensing Letters*, 4(3), 451-455.
- 819 Crow, W. T., G. J. Huffman, R. Bindlish, and T. J. Jackson (2009), Improving satellite-based rainfall accumulation
820 estimates using spaceborne surface soil moisture retrievals, *Journal of Hydrometeorology*, 10(1), 199-212.

821 Daganzo-Eusebio, E., R. Oliva, Y. H. Kerr, S. Nieto, P. Richaume, and S. M. Mecklenburg (2013), SMOS radiometer
822 in the 1400–1427-MHz passive band: Impact of the RFI environment and approach to its mitigation and
823 cancellation, *IEEE Transactions on Geoscience and Remote Sensing*, 51(10), 4999-5007.

824 De Jeu, R. A. M. and M. Owe (2003), Further validation of a new methodology for surface moisture and vegetation
825 optical depth retrieval, *International Journal of Remote Sensing*, 24(22), 4559-4578.

826 De Jeu, R., W. Wagner, T. Holmes, A. Dolman, N. Van De Giesen, and J. Friesen (2008), Global soil moisture patterns
827 observed by space borne microwave radiometers and scatterometers, *Surveys in Geophysics*, 29(4), 399-420.

828 De Jeu, R. A., T. R. Holmes, R. Panciera, and J. P. Walker (2009), Parameterization of the land parameter retrieval
829 model for L-band observations using the NAFE'05 data set, *IEEE Geoscience and Remote Sensing Letters*, 6(4),
830 630-634.

831 Dorigo, W. A., A. Gruber, R. A. M. De Jeu, W. Wagner, T. Stacke, A. Loew, C. Albergel, L. Brocca, D. Chung, R.
832 M. Parinussa, and R. Kidd (2015), Evaluation of the ESA CCI soil moisture product using ground-based
833 observations. *Remote Sensing of Environment*, 162, 380-395.

834 Dorigo, W. A., A. Xaver, M. Vreugdenhil, A. Gruber, A. Hegyiová, A. D. Sanchis-Dufau, D. Zamojski, C. Cordes,
835 W. Wagner, and M. Drusch (2013), Global automated quality control of in situ soil moisture data from the
836 International Soil Moisture Network, *Vadose Zone Journal*, 12(3), vzj2012-0097.

837 Dorigo, W., K. Scipal, R. Parinussa, Y. Liu, W. Wagner, R. De Jeu, and V. Naeimi (2010), Error characterisation of
838 global active and passive microwave soil moisture datasets, *Hydrology and Earth System Sciences*, 14(12), 2605-
839 2616.

840 Dorigo, W., W. Wagner, R. Hohensinn, S. Hahn, C. Paulik, A. Xaver, A. Gruber, M. Drusch, S. Mecklenburg, and P.
841 v. Oevelen (2011), The International Soil Moisture Network: a data hosting facility for global in situ soil moisture
842 measurements, *Hydrology and Earth System Sciences*, 15(5), 1675-1698.

843 Draper, C., J. Walker, P. Steinle, R. De Jeu, and T. Holmes (2009), An evaluation of AMSR-E derived soil moisture
844 over Australia, *Remote Sensing of Environment*, 113(4), 703-710.

845 Draper, C. S., R. H. Reichle, G. J. M. De Lannoy, and Q. Liu (2012), Assimilation of passive and active microwave
846 soil moisture retrievals, *Geophysical Research Letters*, 39(4), L04401.

847 Du, J. (2012), A method to improve satellite soil moisture retrievals based on Fourier analysis, *Geophysical Research*
848 *Letters*, 39(15), L15404.

849 Engman, E. T. (1991), Applications of microwave remote sensing of soil moisture for water resources and agriculture,
850 *Remote Sensing of Environment*, 35(2), 213-226.

851 Entin, J. K., A. Robock, K. Y. Vinnikov, S. E. Hollinger, S. Liu, and A. Namkhai (2000), Temporal and spatial scales
852 of observed soil moisture variations in the extratropics, *Journal of Geophysical Research*, 105(D9), 11865-11877.

853 Ferraro, R. R., C. D. Peters-Lidard, C. Hernandez, F. J. Turk, F. Aires, C. Prigent, X. Lin, S. A. Boukabara, F. A.
854 Furuzawa, K. Gopalan, and K. W. Harrison (2013), An evaluation of microwave land surface emissivities over
855 the continental United States to benefit GPM-era precipitation algorithms. *IEEE Transactions on Geoscience and*
856 *Remote Sensing*, 51(1), 378-398.

857 Foster, G (1996), Wavelets for period analysis of unevenly sampled time series, *The Astronomical Journal*, 112(4),
858 1709-1729.

859 Garcia, D. (2010), Robust smoothing of gridded data in one and higher dimensions with missing values,
860 *Computational Statistics and Data Analysis*, 54(4), 1167-1178.

861 Gouweleeuw, B., A. van Dijk, J. P. Guerschman, P. Dyce, and M. Owe (2012), Space-based passive microwave soil
862 moisture retrievals and the correction for a dynamic open water fraction, *Hydrology and Earth System Sciences*,
863 16(6), 1635-1645.

864 Grody, N. C. (1993), Remote sensing of the atmosphere from satellites using microwave radiometry. In *Atmospheric*
865 *remote sensing by microwave radiometry*, Editor: Michael A. Janssen, 259-334.

866 Gruber, A., W. Dorigo, S. Zwieback, A. Xaver, and W. Wagner (2013), Characterizing coarse-scale representativeness
867 of in situ soil moisture measurements from the International Soil Moisture Network, *Vadose Zone Journal*, 12(2):
868 vjz2012-0170.

869 Holmes, T. R. H., W. T. Crow, C. Hain, M. C. Anderson, and W. P. Kustas (2015), Diurnal temperature cycle as
870 observed by thermal infrared and microwave radiometers. *Remote Sensing of Environment*, 158, 110-125.

871 Holmes, T., R. De Jeu, M. Owe, and A. Dolman (2009), Land surface temperature from Ka band (37 GHz) passive
872 microwave observations, *Journal of Geophysical Research: Atmospheres*, 114, D04113.

873 Jackson, T. J., T. J. Schmugge, and J. R. Wang (1982), Passive microwave sensing of soil moisture under vegetation
874 canopies. *Water Resources Research*, 18(4), 1137-1142.

875 Jackson, T. J., M. H. Cosh, R. Bindlish, P. J. Starks, D. D. Bosch, M. Seyfried, D. C. Goodrich, M. S. Moran, and J.
876 Du (2010), Validation of advanced microwave scanning radiometer soil moisture products, *IEEE Transactions*
877 *on Geoscience and Remote Sensing*, 48(12), 4256-4272.

878 Katul, G. G., A. Porporato, E. Daly, A. C. Oishi, H. S. Kim, P. C. Stoy, J. Y. Juang, and M. B. Siqueira (2007), On
879 the spectrum of soil moisture from hourly to interannual scales, *Water Resources Research*, 43(5), 1-10.

880 Kim, S., Y. Liu, F. M. Johnson, R. M. Parinussa, and A. Sharma (2015), A global comparison of alternate AMSR2
881 soil moisture products: Why do they differ?, *Remote Sensing Environment*, 161, 43-62.

882 Komma, J., G. Blöschl, and C. Reszler (2008), Soil moisture updating by Ensemble Kalman Filtering in real-time
883 flood forecasting, *Journal of Hydrology*, 357(3), 228-242.

884 Koster, R. D., P. A. Dirmeyer, Z. Guo, G. Bonan, E. Chan, P. Cox, C. Gordon, S. Kanae, E. Kowalczyk, and D.
885 Lawrence (2004), Regions of strong coupling between soil moisture and precipitation, *Science*, 305(5687), 1138-
886 1140.

887 Lacava, T., V. Cuomo, E. V. Di Leo, N. Pergola, F. Romano, and V. Tramutoli (2005), Improving soil wetness
888 variations monitoring from passive microwave satellite data: the case of April 2000 Hungary flood, *Remote*
889 *Sensing of Environment*, 96(2), 135-148.

890 Lakhankar, T., N. Krakauer, and R. Khanbilvardi (2009a), Applications of microwave remote sensing of soil moisture
891 for agricultural applications, *International Journal of Terraspace Science and Engineering*, 2(1), 81-91.

892 Lakhankar, T., H. Ghedira, M. Temimi, A. E. Azar, and R. Khanbilvardi (2009b), Effect of land cover heterogeneity
893 on soil moisture retrieval using active microwave remote sensing data. *Remote Sensing*, 1(2), 80-91.

894 Li, L., E. G. Njoku, E. Im, P. S. Chang, and K. S. Germain (2004), A preliminary survey of radio-frequency
895 interference over the US in Aqua AMSR-E data, *IEEE Transactions on Geoscience and Remote Sensing*, 42(2),
896 380-390.

897 Lin, B., B. Wielicki, P. Minnis, and W. Rossow (1998), Estimation of water cloud properties from satellite microwave,
898 infrared and visible measurements in oceanic environments: 1. Microwave brightness temperature simulations.
899 *Journal of Geophysical Research: Atmospheres*, 103(D4), 3873-3886.

900 Loew, A. (2008), Impact of surface heterogeneity on surface soil moisture retrievals from passive microwave data at
901 the regional scale: The Upper Danube case. *Remote Sensing of Environment*, 112(1), 231-248.

902 Lomb, N. R. (1976), Least-squares frequency analysis of unequally spaced data, *Astrophysics and Space Science*,
903 39(2), 447-462.

904 Meesters, A. G., R. A. De Jeu, and M. Owe (2005), Analytical derivation of the vegetation optical depth from the
905 microwave polarization difference index, *IEEE Geoscience and Remote Sensing Letters*, 2(2), 121-123.

906 Mo, T., B. Choudhury, T. Schmugge, J. Wang, and T. Jackson (1982), A model for microwave emission from
907 vegetation-covered fields, *Journal of Geophysical Research: Oceans*, 87(C13), 11229-11237.

908 Moody, A., and D. M. Johnson (2001), Land-surface phenologies from AVHRR using the discrete Fourier transform,
909 *Remote Sensing of Environment*, 75(3), 305-323.

910 Njoku, E. G., T. J. Jackson, V. Lakshmi, T. K. Chan, and S. V. Nghiem (2003), Soil moisture retrieval from AMSR-
911 E, *IEEE Transactions on Geoscience and Remote Sensing*, 41(2), 215-229.

912 Njoku, E. G., P. Ashcroft, T. K. Chan, and L. Li (2005), Global survey and statistics of radio-frequency interference
913 in AMSR-E land observations, *IEEE Transactions on Geoscience and Remote Sensing*, 43(5), 938-947.

914 Owe, M., R. de Jeu, and J. Walker (2001), A methodology for surface soil moisture and vegetation optical depth
915 retrieval using the microwave polarization difference index, *IEEE Transactions on Geoscience and Remote
916 Sensing*, 39(8), 1643-1654.

917 Owe, M., R. de Jeu, and T. Holmes (2008), Multisensor historical climatology of satellite-derived global land surface
918 moisture, *Journal of Geophysical Research: Earth Surface (2003-2012)*, 113, F01002.

919 Parinussa, R. M., A. G. C. A. Meesters, Y. Liu, W. Dorigo, W. Wagner, and R. A. M. De Jeu (2011), Error estimates
920 for near-real-time satellite soil moisture as derived from the land parameter retrieval model, *Geoscience and
921 Remote Sensing Letters, IEEE*, 8(4), 779-783.

922 Prigent, C., F. Aires, and W. B. Rossow (2006), Land surface microwave emissivities over the globe for a decade.
923 *Bulletin of the American Meteorological Society*, 87(11), 1573-1584.

924 Rebel, K., R. De Jeu, P. Ciais, N. Viovy, S. Piao, G. Kiely, and A. Dolman (2012), A global analysis of soil moisture
925 derived from satellite observations and a land surface model, *Hydrology and Earth System Sciences*, 16, 833-
926 847.

927 Reichle, R. H., and R. D. Koster (2005), Global assimilation of satellite surface soil moisture retrievals into the NASA
928 Catchment land surface model, *Geophysical Research Letters*, 32(2), L02404.

929 Reichle, R. H., R. D. Koster, J. Dong, and A. A. Berg (2004), Global soil moisture from satellite observations, land
930 surface models, and ground data: Implications for data assimilation, *Journal of Hydrometeorology*, 5(3), 430-
931 442.

932 Reichle, R. H., R. D. Koster, P. Liu, S. P. Mahanama, E. G. Njoku, and M. Owe (2007), Comparison and assimilation
933 of global soil moisture retrievals from the Advanced Microwave Scanning Radiometer for the Earth Observing
934 System (AMSR-E) and the Scanning Multichannel Microwave Radiometer (SMMR), *Journal of Geophysical*
935 *Research: Atmospheres*, 112(D9), 9108.

936 Scargle, J. D. (1982), Studies in astronomical time series analysis. II-Statistical aspects of spectral analysis of unevenly
937 spaced data, *The Astrophysical Journal*, 263, 835-853.

938 Scharlemann, J. P., D. Benz, S. I. Hay, B. V. Purse, A. J. Tatem, G. W. Wint, and D. J. Rogers (2008), Global data
939 for ecology and epidemiology: a novel algorithm for temporal Fourier processing MODIS data, *PloS one*, 3(1),
940 e1408.

941 Seneviratne, S. I., T. Corti, E. L. Davin, M. Hirschi, E. B. Jaeger, I. Lehner, B. Orlowsky, and A. J. Teuling (2010),
942 Investigating soil moisture-climate interactions in a changing climate: A review, *Earth Science Reviews*, 99(3),
943 125-161.

944 Srivastava, P. K., D. Han, M. A. R. Ramirez, and T. Islam (2013), Appraisal of SMOS soil moisture at a catchment
945 scale in a temperate maritime climate, *Journal of Hydrology*, 498, 292-304.

946 Su, C. H., D. Ryu, A. W. Western, and W. Wagner (2013a), De-noising of passive and active microwave satellite soil
947 moisture time series, *Geophysical Research Letters*, 40(14), 3624-3630.

948 Su, C. H., D. Ryu, R. I. Young, A. W. Western, and W. Wagner (2013b), Inter-comparison of microwave satellite soil
949 moisture retrievals over the Murrumbidgee Basin, southeast Australia, *Remote Sensing of Environment*, 134, 1-
950 11.

951 Su, C. H., S. Y. Narsey, A. Gruber, A. Xaver, D. Chung, D. Ryu, and W. Wagner (2015), Evaluation of post-retrieval
952 de-noising of active and passive microwave satellite soil moisture, *Remote Sensing of Environment*, 163, 127-
953 139.

954 Van der Schalie, R., R. Parinussa, L. J. Renzullo, A. Van Dijk, C.-H. Su, and R. A. de Jeu (2015), SMOS soil moisture
955 retrievals using the land parameter retrieval model: Evaluation over the Murrumbidgee Catchment, southeast
956 Australia, *Remote Sensing of Environment*, 163, 70-79.

957 Van der Schalie, R., Y. Kerr, J. Wigneron, N. Rodríguez-Fernández, A. Al-Yaari, and R. de Jeu (2016), Global SMOS
958 soil moisture retrievals from the land parameter retrieval model, *International Journal of Applied Earth*
959 *Observation and Geoinformation*, 45, 125-134.

960 Wagner, W., G. Blöschl, P. Pampaloni, J. C. Calvet, B. Bizzarri, J. P. Wigneron, and Y. Kerr (2007a), Operational
961 readiness of microwave remote sensing of soil moisture for hydrologic applications, *Hydrology Research*, 38(1),
962 1-20.

963 Wagner, W., V. Naeimi, K. Scipal, R. de Jeu, and J. Martínez-Fernández (2007b), Soil moisture from operational
964 meteorological satellites, *Hydrogeology Journal*, 15(1), 121-131.

- 965 Walker, J. P., and P. R. Houser (2004), Requirements of a global near-surface soil moisture satellite mission: accuracy,
966 repeat time, and spatial resolution, *Advances in Water Resources*, 27(8), 785-801.
- 967 Wang, G., D. Garcia, Y. Liu, R. de Jeu, and A. J. Dolman (2012), A three-dimensional gap filling method for large
968 geophysical datasets: Application to global satellite soil moisture observations, *Environmental Modelling and*
969 *Software*, 30, 139-142.
- 970 Wang, J., and B. Choudhury (1981), Remote sensing of soil moisture content, over bare field at 1.4 GHz frequency,
971 *Journal of Geophysical Research: Oceans*, 86(C6), 5277-5282.
- 972 Wang, J. R., and T. J. Schmugge (1980), An empirical model for the complex dielectric permittivity of soils as a
973 function of water content, *IEEE Transactions on Geoscience and Remote Sensing*, 4(GE-18), 288-295.
- 974 Weng, F. (2010), Observations and simulations of microwave land emissivity. European Centre for Medium-Range
975 Weather Forecasts — Joint Center for Satellite Data Assimilation (ECMWF—JCSDA) Workshop, June 15-17,
976 Reading, UK.
- 977 Wu, W., and R. E. Dickinson (2004), Time Scales of Layered Soil Moisture Memory in the Context of Land-
978 Atmosphere Interaction, *Journal of Climate*, 17(14), 2752-2764.